


Observational hints on the torus obscuring gas behaviour through X-rays with *NuSTAR* data

N. Osorio-Clavijo,¹  O. González-Martín,¹ S.F. Sánchez,² D. Esparza-Arredondo,¹ J. Masegosa,³ C. Victoria-Ceballos,¹ L. Hernández-García^{4,5} Y. Díaz,⁵

¹*Instituto de Radioastronomía and Astrofísica (IRyA-UNAM), 3-72 (Xangari), 8701, Morelia, Mexico*

²*Instituto de Astronomía, Universidad Nacional Autónoma de México, A. P. 70-264, C.P. 04510, México, D.F., Mexico*

³*IAA – Instituto de Astrofísica de Andalucía (CSIC), Glorieta de la Astronomía, 18008 Granada, Spain*

⁴*Millennium Institute of Astrophysics (MAS), Nuncio Monseñor Sótero Sanz 100, Providencia, Santiago, Chile*

⁵*Instituto de Física y Astronomía, Facultad de Ciencias, Universidad de Valparaíso, Gran Bretaña 1111, Playa Ancha, Valparaíso, Chile*

Accepted 2021 December 19. Received 2021 December 16; in original form 2021 March 25.

ABSTRACT

According to theory, the torus of active galactic nuclei (AGN) is sustained from a wind coming off the accretion disk, and for low efficient AGN, it has been proposed that such structure disappears. However, the exact conditions for its disappearance remain unclear. This can be studied throughout the reflection component at X-rays, which is associated with distant and neutral material at the inner walls of the torus in obscured AGN. We select a sample of 81 AGNs observed with *NuSTAR* with a distance limit of $D < 200$ Mpc and Eddington rate $\lambda_{\text{Edd}} \equiv L_{\text{bol}}/L_{\text{Edd}} < 10^{-3}$. We fit the 3–70 keV spectra using a model accounting for a partial-covering absorber plus a reflection component from neutral material. We find that the existence of the reflection component spans in a wide range of black-hole mass and bolometric luminosities, with only $\sim 13\%$ of our sample (11 sources) lacking of any reflection signatures. These sources fall in the region in which the torus may be lacking in the L-MBH diagram. For the sources with a detected reflection component, we find that the vast majority of them are highly obscured ($\log N_{\text{H}} > 23$), with $\sim 20\%$ being Compton-thick. We also find an increase on the number of unobscured sources and a tentative increase on the ratio between $\text{FeK}\alpha$ emission line and Compton-hump luminosities toward $\lambda_{\text{Edd}} = 10^{-5}$, suggesting that the contribution of the $\text{FeK}\alpha$ line changes with Eddington ratio.

Key words: galaxies: active - X-rays: galaxies - galaxies: Seyfert.

1 INTRODUCTION

It has been widely accepted that most galaxies with bulges host a super massive black-hole (SMBH), sometimes fed by an accretion disk, causing the release of energy in orders of magnitude that can go up to $L_{\text{bol}} \sim 10^{47}$ erg s⁻¹ (see [Netzer 2015](#), for a review). Such objects are known as Active Galactic Nuclei (AGN). The Unified Model (UM) of AGN ([Antonucci 1993](#); [Urry & Padovani 1995](#)) assumes that all AGN have the same components (accretion disk, broad and narrow line regions, a dusty structure-the torus and, in some cases a jet) and that the difference in the spectrum relies on the angle of sight to the observer. This effect may prevent the observer to see the inner parts of AGN and therefore the existence/absence of broad lines in the optical spectrum, leading to a purely observational classification (see [Netzer 2015](#); [Ramos Almeida and Ricci 2017](#), for recent reviews on the topic).

The cornerstone of the UM are both the obscuring structure and the inclination angle, as well as the existence of the jet. However, some observations suggest that there are objects lacking the obscuring structure (the so-called true type 2 AGN, [Laor 2003](#)). This might

be explained under the theoretical prediction that the torus should disappear below a certain luminosity, assuming that both the torus and broad line region (BLR) are formed from a wind coming off the accretion disk ([Elvis 2000](#)). In fact, [Elitzur and Shlosman \(2006\)](#) state that both the torus and the BLR should disappear for bolometric luminosities below ($L_{\text{bol}} \sim 10^{42}$ erg s⁻¹), since the radiation pressure cannot longer counteract the gravity for both structures. Indeed, [González-Martín et al. \(2017\)](#) using mid-infrared (mid-IR) spectra, have found hints on the torus disappearance in inefficient AGN (see also [González-Martín et al. 2015](#)). Moreover, [Elitzur and Ho \(2009\)](#) find that the torus might still be absent for luminous AGN, depending on the efficiency of the accretion disk at feeding the SMBH. Therefore, not only the luminosity of the AGN gives us hints on the existence of the torus, but also the efficiency and density of the wind. Both mid-IR and X-ray studies suggest that the torus is intrinsically different in type-2 AGN than in type-1 AGN (e.g., [Ramos Almeida et al. 2009](#); [Ricci et al. 2011](#)), and that the fraction of type-2 sources increases for AGN with Eddington rates $\lambda_{\text{Edd}} \equiv L_{\text{bol}}/L_{\text{Edd}} \approx 0.001$ ([Ricci et al. 2017](#)). Indeed, [Khim and Yi \(2017\)](#) found a complex behaviour where the number of clouds and covering factor change for high accretion sources (i.e., $0.01 < \lambda_{\text{Edd}} < 1$), forming a ridge-shaped distribution in the luminosity versus black-hole mass (M_{BH})

* e-mail: n.osorio@irya.unam.mx

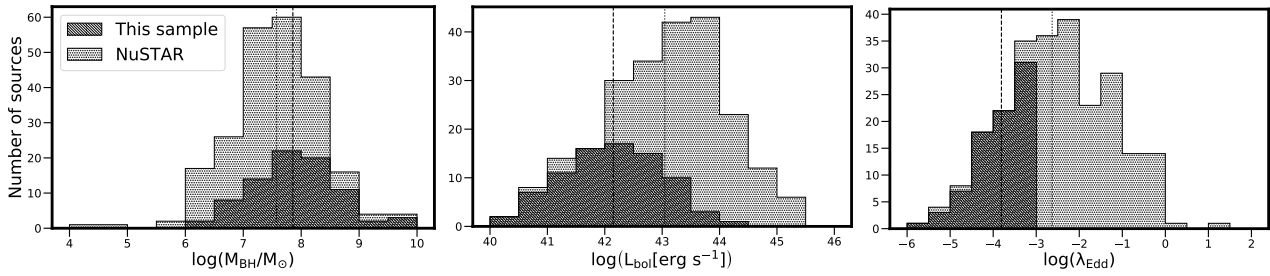


Figure 1. Histograms of the distribution of M_{BH} (left), L_{bol} (center) and λ_{Edd} (right), for the final sample (dashed, 81 sources) versus the full sample with M_{BH} measurements (dotted, 231 sources). The dashed and dotted vertical lines in each panel represent the mean value of the parameter in the X axis for both the final and full samples, respectively. Note that in the left panel, six sources fulfill the accretion criterion but are still excluded from the analysis because they are classified as starburst or because they are at the center of clusters (see text).

diagram. However, the behaviour of the torus for low accretion AGN with $\lambda_{\text{Edd}} < 0.001$, where the torus should evolve to its disappearance, remains an open question.

Historically, the obscuring matter has been studied through the column density along the line of sight (LOS) that affects the primary X-ray continuum (e.g. [Matt, Guainazzi, and Maiolino 2003](#)). Additionally, the torus can also be studied at X-rays because the inner parts of it can reflect the X-ray emission from the corona above the disk, placing a reflection component in the X-ray spectrum. This reflection component has two main signatures: the Compton hump and the $\text{FeK}\alpha$ line. Theoretical works have shown that the resulting reflection spectrum depends on the shape and distribution of the reflector, but also on the line-of-sight to the observer, and all of this might have an impact on the luminosity of this component (e.g. see [Furui et al. 2016](#)). However, it has not been until recent years that studies aiming to detect and characterize the torus through the reflection component at X-rays have been developed (e.g. [Ricci et al. 2011](#); [Liu and Li 2014](#); [Ricci et al. 2014](#); [Furui et al. 2016](#); [Kawamuro et al. 2016](#)), but also thanks to the unprecedented sensitivity achieved above 10 keV provided by *NuSTAR* (e.g., [Panagiotou and Walter 2019, 2020](#); [Esparza-Arredondo et al. 2019, 2021](#), among others).

The aim of this study is to trace the behaviour of the obscuring material and plausible disappearance of the torus through X-rays for low accretion AGN, compared to what has already been found for more efficient AGN, by using *NuSTAR* data. This work is divided as follows: in Section 2 we present the sample and the data reduction. In Section 3 we present the model and the spectral analysis, while in Section 4 we present the results obtained, in Section 5 we discuss them and finally we present the summary and conclusions of our work in Section 6. Throughout the analysis, we assume a cosmology of $H_0 = 70 \text{ km s}^{-1} \text{ Mpc}^{-1}$, $q_0 = 0$ and $\Omega_{\lambda_0} = 0.73$, and all distances are redshift-independent taken from the NASA Extragalactic Database (NED¹).

2 SAMPLE AND DATA REDUCTION

2.1 Sample selection

We search for all available galaxies within a 10 arcmin radius (using SIMBAD database²) for all archived pointings within the *NuSTAR* database (until July 2020). We find a total of 1313 galaxies within a

distance of 200 Mpc ($z < 0.05$) to sample the nearby Universe. We then retrieve the activity type, keeping only those galaxies classified as AGN in either NED or SIMBAD databases. We obtain a total of 463 AGN. We download all the data from the HEASARC archive³ and reduce the observations for these 463 AGN (see section 2.2 reduction procedure), keeping only the observations with more than 30 bins after producing grouped spectra, and at least 10 bins above 10 keV. We also remove from the sample those AGN where the *NuSTAR* resolution cannot fully isolate the nuclear spectra for dual AGN. We obtain a total of 301 sources fulfilling these criteria.

We finally search for M_{BH} . These measurements are needed to obtain an estimate of the Eddington rate. We firstly look for M_{BH} calculated via reverberation mapping (e.g. [Laor 2001, 2003](#); [Woo and Urry 2002](#); [Vasudevan and Fabian 2009](#)) and velocity dispersion otherwise (e.g. [McKernan, Ford, and Reynolds 2010](#); [van den Bosch et al. 2015](#); [van den Bosch 2016](#)), by using the M - σ relation, $M_{\text{BH}} (\log(M_{\text{BH}}/M_{\odot}) = 8.27 + 5.1 \log(\sigma/200 \text{ km s}^{-1})$ [Ferrarese and Merritt 2000](#); [Gebhardt et al. 2000](#)). As for the sources for which the M_{BH} is not calculated through the methods reported above, we also search for the M_{BH} in different AGN catalogues where the mass are compiled from literature (e.g. [Khorunzhev et al. 2012](#); [Koss et al. 2017](#); [Bär et al. 2019](#)). We obtain measurements for 231 out of the 301 AGN. This sample is now referred to as full sample.

We then fit the spectra of the 231 AGN with an unabsorbed power-law to roughly calculate the bolometric luminosity, L_{bol} , from X-rays following the $L_{\text{bol}}/L_{(2-10 \text{ keV})}$ conversion from [Marconi et al. \(2004\)](#), where L_{bol} is in units of L_{\odot} :

$$\log[L_{\text{bol}}/L_{(2-10 \text{ keV})}] = 1.54 + 0.24(L_{\text{bol}} - 12) + 0.012(L_{\text{bol}} - 12)^2 - 0.0015(L_{\text{bol}} - 12)^3. \quad (1)$$

We define low accretion sources as those with $\lambda_{\text{Edd}} < 10^{-3}$, where L_{Edd} is the Eddington luminosity, defined as the maximum luminosity an object can release without losing the thermal equilibrium. Such definition is based on the assumption that the transition from the standard disk ([Shakura and Sunyaev 1973](#)) to an Advection Dominated Accretion disk (ADAF, [Narayan and Yi 1995](#)) occurs around this value (see also, [Constantin et al. 2009](#); [Gu & Cao 2009](#); [Younes et al. 2011](#); [Gültekin et al. 2012](#); [Jang et al. 2014](#); [Connolly et al. 2016](#); [Hernández-García et al. 2016](#)). This sample contains a total of 87 sources. This corresponds to $\sim 20\%$ of the total nearby available AGN observed with *NuSTAR*. Four of these sources (NGC 3310, Mrk 18, Arp 299C, and M 83) are excluded from the sample because

¹ <https://ned.ipac.caltech.edu/>

² <http://simbad.u-strasbg.fr/simbad/>

³ <https://heasarc.gsfc.nasa.gov/>

Name	Other name	ra	dec	Redshift	Dist.	log M_{BH}	AGN	Galaxy	Obs. date	Obs ID	Exp. time	Ext. radius	N. counts	Bins
(1)	(2)	deg	deg	(5)	Mpc	(7)	(8)	(9)	(10)	(11)	ks	arcmin	(14)	(15)
NGC1052	PKS0238-084	40.26999	-8.25576	0.0048	20.6	8.4	L2	E4	2017-01-17	60201056002	59.75	0.5	91.27	738
NGC2655	ARP225	133.90721	78.22308	0.0057	24.4	8.0	L2	Sa-0	2016-11-10	60160341004	15.95	2	35.30	98
UGC5101	CGCG289-011	143.96539	61.35292	0.0394	168.6	8.3	L1	S?	2014-03-21	60001068002	18.29	1	24.33	51
M81	NGC3031	148.88822	69.06530	0.0009	3.7	7.8	L1.8	SAab	2015-05-18	60101049002	209.09	0.5	255.69	1252
NGC3079	UGC05387	150.49085	55.67979	0.0038	16.4	7.2	L2	SBc	2013-11-12	60061097002	21.54	0.5	29.85	128
UGC5881	CGCG125-008	161.67715	25.93155	0.0206	88.2	8.2	L2	Sa	2015-05-17	60160409002	21.41	1	37.39	169
NGC3628	UGC06350	170.07091	13.58949	0.0023	9.8	7.2	L2	SAb	2017-12-23	60371004002	50.35	1	32.46	86
NGC3718	ARP214	173.14522	53.06791	0.0034	14.7	8.3	L1	SB	2017-10-27	60301031004	90.37	0.5	44.38	208
NGC3998	UGC06946	179.48389	55.45359	0.0047	20.1	9.0	L1.9	Sa-0	2016-10-25	60201050002	103.94	0.5	111.02	714
NGC4102	UGC07096	181.59631	52.71095	0.0046	19.5	8.2	L2	SAB	2015-11-19	60160472002	20.57	0.5	39.14	198
M106	NGC4258	184.74008	47.30372	0.0017	7.3	7.5	L1.9	SBbc	2016-01-10	60101046004	103.62	0.5	71.20	466
M58	NGC4579	189.43165	11.81809	0.0043	18.4	7.9	L1.9	Sb	2016-12-06	60201051002	117.84	0.5	116.60	738
NGC5005	UGC08256	197.73463	37.05894	0.0047	20.1	8.1	L1.9	SABb	2014-12-16	60001162002	49.70	1	27.82	40
NGC6240	IC4625	253.24525	2.40099	0.0245	104.8	9.1	L2	S0-a	2014-03-30	60002040002	30.86	0.5	55.62	444
MCG+08-31-041	ARP102B	259.81038	48.98040	0.0242	103.5	8.9	L1	E0	2015-11-24	60160662002	22.40	1	45.28	248
NGC7130	IC5135	327.08121	-34.95131	0.0162	69.2	7.5	L2	Sa	2016-12-15	60261006002	42.12	0.5	23.86	63
NGC7331	UGC12113	339.26709	34.41592	0.0031	13.4	7.8	L2	Sbc	2016-05-03	40202013002	42.97	1	38.16	153
NGC7479	UGC12343	346.23612	12.32288	0.0066	28.3	7.3	L1.9	SBbc	2016-05-12	60201037002	18.45	1	27.73	82

Table 1. Observational parameters for the LINER sample. (1) Name of the source; (2) other name (3) right ascension; (4) declination; (5) Redshift; (6) Redshift-independent distance in Mpc; (7) $\log(M_{\text{BH}}/M_{\odot})$; (8) AGN classification; (9) Galaxy type. All galaxy types were retrieved from NED; (10) date of the observation; (11) Observation ID in *NuSTAR*; (12) Exposure time of the observation in ksec; (13) is the extraction radius used in the data reduction; (14) is the number of counts in the 3–60 keV *NuSTAR* band when accounting for the background subtraction; and (15) is the number of bins. In columns (1) and (2), 2MXJ (2MXIJ) is abbreviation for 2MASXJ (2MASXIJ), 2M is the abbreviation for 2MASS and W is the abbreviation for WISE.

although they are classified as AGN in SIMBAD/NED, they are also classified as starbursts. Finally, we exclude NGC 4486 due to the strong thermal and jet contribution (de Jong *et al.* 2015), while we exclude Centaurus A due to strong jet contribution (Hardcastle *et al.* 2003). Note that we also check for important thermal/jet contribution for the rest of the sample. Although in some cases there are reported thermal contribution at X-rays (see González-Martín *et al.* 2009), it does not contribute above 3 keV for the rest of the sources. One consequence, although not the only one, would be a very steep photon index (i.e., $\Gamma > 2$ Nemmen, Storchi-Bergmann, and Eracleous 2014) as the one in M 87 ($\Gamma = 2.8 \pm 0.4$ de Jong *et al.* 2015), which is not the case in our sample, see section 4). Our final sample comprises a total of 81 sources.

Fig. 1 shows the distribution (in logarithmic scale) of M_{BH} (left), L_{bol} (center) and λ_{Edd} (right) for our final sample of 81 sources, compared to the full sample of 231 sources with M_{BH} estimates. The mean of the distributions of the final sample for M_{BH} , L_{bol} and λ_{Edd} are $< \log(M_{\text{BH}}) > = 7.9$, $< \log(L_{\text{bol}}) > = 42.1$ and $\log(\lambda_{\text{Edd}}) = 3.8$, compared to $< \log(M_{\text{BH}}) > = 7.6$, $< \log(L_{\text{bol}}) > = 43.0$ and $< \log(\lambda_{\text{Edd}}) > = 2.6$, for the full sample. Thus, our final sample contains lower luminosity AGN with roughly the same range of M_{BH} values compared to the full sample. Note that this imposes a bias on our sample for Eddington rates above $\log(\lambda_{\text{Edd}}) > -3$. Moreover, once we correct by absorption in the line-of-sight, Eddington rates will be higher (see section 4.1). Thus, we might lack objects with low obscuration and intrinsically high Eddington rate above $\log(\lambda_{\text{Edd}}) > -2.5$. Another source of bias is the fact that our sample relies purely on archival data. For instance, we do not find available *NuSTAR* data for the candidates of torus disappearance in González-Martín *et al.* (2017). Thus, we might also be missing the least luminous sources as they might not have been observed yet. We warn the reader on the fact that our sample is by no means complete, although it does cover a wide range in M_{BH} and Eddington rate.

Several works have studied samples of inefficient AGN in different wavelengths aiming to understand the nature and behaviour of the reflection component and will be used to compare with our new results along the text. Here we report a brief summary on the matching of our sample with theirs. The largest sample using X-rays is reported by González-Martín *et al.* (2009) where they study a sample of 82

inefficient AGN using *Chandra* and *XMM-Newton* data. We have 12 sources in common with available *NuSTAR* observations. Kawamuro *et al.* (2016) also studied a sample of 10 inefficient AGN using *Suzaku* and we have five sources in common with them. On the other hand, González-Martín *et al.* (2017) analyzed a sub-sample of those presented by González-Martín *et al.* (2009) together with a complementary Seyfert sample (22 sources). We have a total of 39 sources in common with the works mentioned above, which is around 50% of our final sample.

Tables 1 and 2 report the observational parameters for the optically classified as low ionization nuclear emission-line regions (LINER, 18 sources) and Seyfert (64 sources) samples, respectively.

2.2 Data reduction

All *NuSTAR* (Harrison *et al.* 2013) data were reduced using the data analysis software *NuSTARDAS* v.1.4.4 distributed by the High Energy Astrophysics Archive Research Center (HEASARC). The calibrated, cleaned and screened event files for both FPMA and FMPB focal plane modules were generated using the *NUPIPELINE* task (CALDB 20160502). We automatically extracted three circular apertures with radius of 0.5, 1, and 2 arcsec centred at the NED position of the source. For each of them we produced eight backgrounds around the target. These backgrounds are located at a distance of three times the aperture radius of the target (i.e. 1.5, 3, or 6 arcsec) with position angles of 0, 45, 90, 135, 180, 225, 270, and 315 degrees. We produced in this way 24 spectra for each target. The Redistribution Matrix and Auxiliary Response files (RMF and ARF) were produced with the *NUPRODUCTS* package available in *NuSTARDAS*. We chose the spectrum that maximises the S/N in the 3–70 keV band, avoiding off-nuclear contributors. Tables 1 and 2 provide the best extraction radius for each target. Note the optimal extraction radius is ~ 1 arcmin ($D \simeq [1 - 52]$ kpc) for the vast majority of the objects, due to the relative faintness of our sources.

We then performed a binning method with a minimum S/N ratio of 3, using the *FTGROUPPHA* task within *FTOOLS*. The grouping using a minimum S/N ratio is particularly relevant for faint sources which are probably background dominated above ~ 25 keV. Note that we also performed the standard grouping method accounting for a minimum

In the software terminology, this model has the following form:

$$M_1 = \text{phabs}_{\text{Gal}}((\text{zphabs}_{\text{intr}} * \text{zpowerlw}) + \text{ct} * \text{zpowerlw} + \text{zgauss}_{6.7 \text{ keV}} + \text{zgauss}_{6.97 \text{ keV}}) \quad (2)$$

where $(\text{zphabs}_{\text{intr}} * \text{zpowerlw}) + \text{ct} * \text{zpowerlw}$ represents the partial-covering scenario, in which the first power-law component is associated with the intrinsic continuum absorbed by the material along the LOS to the observer and the second power-law component is the scattered emission that reaches the observer. The parameters for both power-laws are linked, including the normalization, to simulate the partial-covering scenario. The free parameters for this model are the column density (N_{H}), the constant associated with the covering factor (as $\text{ct} = 1 - f_{\text{cov}}$), the photon index (Γ_{pl}), and the normalization of the power-law. The free parameters of the Gaussian components, emulating the emission lines are the center, width and normalization. The widths of the Gaussian components are fixed to be narrow (0.1 keV⁵) and the centers are fixed to 6.7 and 6.97 keV, respectively.

For the second and third models we include an extra reflection component as follows:

$$M_2 = M_1 + \text{phabs}_{\text{Gal}}(\text{pexrav} + \text{zgauss}_{6.4 \text{ keV}}) \quad (3)$$

$$M_3 = M_1 + \text{phabs}_{\text{Gal}}(\text{pexmon}) \quad (4)$$

For M_2 , we choose as reflection component the `pexrav` model (Magdziarz and Zdziarski 1995). This model assumes Compton reflection from neutral X-ray photons in an optically thick material with plane-parallel geometry. This model has as free parameters the photon index, high energy cutoff, relative reflection (R), metal and iron abundances, inclination angle, and normalization. We have set the photon index of `pexrav` (Γ_{pex}) to be the same as that of the power-law, assuming that the reflection occurs in the AGN such that both emissions are correlated. The energy cutoff is fixed to 300 keV assuming this cutoff to happen above the *NuSTAR* energy range. Note that although several works (e.g. Molina *et al.* 2019; Younes *et al.* 2019; Ezhikode *et al.* 2020) have aimed to find this cutoff in AGN spectra, it has only been possible for very few objects, and in most cases, it happens well above the *NuSTAR* range (e.g. Baloković *et al.* 2020). Therefore, we do not expect for this parameter to be constrained nor to affect the overall analysis. We have set R to -1 for `pexrav` to account for the reflection component only, without contribution from the intrinsic power-law continuum. Thus, this reflection model with the relative reflection set to -1 plus the power-law component is equivalent to the `pexrav` allowing the relative reflection to vary. However, we used with the relative reflection to -1 in order to separate both the intrinsic continuum and the reflection components.

The rest of the parameters are set to their default values except for the normalization. Note that in this model version, the addition of an extra Gaussian profile is necessary to emulate the $\text{FeK}\alpha$ line, since `pexrav` assumes reflection from a neutral material, and does not account for this line. In this model, the width of the line at 6.4 keV is also fixed to 0.1 keV.

For M_3 , we include the reflection component using `pexmon` (Nandra *et al.* 2007). This model is an updated version of `pexrav` that includes fluorescence lines such as $\text{FeK}\alpha$, $\text{FeK}\beta$ and $\text{NiK}\alpha$. This model also accounts for the Compton shoulder, by assuming a Gaussian line at 6.315 keV with a width of 0.35 keV. Additionally, it assumes a connection between the equivalent width (EW) of the $\text{FeK}\alpha$

line and that of the Compton shoulder. This reflection model has as free parameters the photon index (Γ_{pex}), relative reflection, cutoff energy, metal and iron abundances, inclination angle, and normalization. Similar to M_2 , the parameter R is set to -1 , the energy cutoff is set to 300 keV and the other parameters, except the normalization, are set to their default values.

The difference between M_2 and M_3 relies on the fact that `pexmon` accounts for the abundance of iron in the medium through the inclusion of the $\text{FeK}\alpha$, $\text{FeK}\beta$ and $\text{NiK}\alpha$ lines. Indeed, these lines are correlated with the Compton-reflection as they are fixed to a fraction of the Compton-shoulder, and they also depend on the photon index of the intrinsic continuum. `pexmon` also accounts for the Compton-shoulder, while `pexrav` is a simpler model not accounting for such features. Thus, `pexmon` already incorporates the $\text{FeK}\alpha$ line at 6.4 keV while we add this line using a Gaussian profile in M_2 . We use M_2 to calculate the EW and luminosity of the 6.4 keV line, with the normalization and error of the line component and the tools `EQUIVALENT` and `LUMINOSITY` within `XSPEC`. M_2 also allows us to isolate the effect of the line from that of the Compton shoulder. Note that both models are equivalent in the analysis. However, since `pexmon` self-consistently accounts for both the continuum and line emission due to the reprocessing in neutral, distant material, the rest of the analysis is based on this model. We include M_1 to study the detection of the reflection component in our sample through the f-statistic test when comparing models (see below). Note also that regardless of the model, we account for Galactic absorption and redshift by using the `NH` tool within `FTOOLS` (retrieved from NED⁶ and fixed to the HI maps of Kalberla *et al.* 2005).

We also use a fourth model that accounts for reflection dominated sources, i.e., sources for which the intrinsic continuum is completely covered by the reflection component in the available X-ray data. This model has the following form:

$$M_4 = \text{phabs}_{\text{Gal}} * \text{pexmon} \quad (5)$$

This analysis does not use sophisticated models as `BORUS` (Baloković *et al.* 2018) or `MYTORUS` (Murphy and Yaqoob 2009) for neutral torus reflection because the faintness of the sources in our sample may not allow us to restrict geometrical parameters for the majority of them. Indeed, we also tested the `MYTORUS` model, but the S/N of the data were too low for parameters to be restricted in most cases. Instead, we prefer a homogeneous analysis of the strength and general characteristics of the reflection component in our sample. This is sufficient to study the dependence of the existence of the reflection component with the AGN power, which is one of the main purposes of this analysis. Furthermore, it also avoids the use of ionized disk reflection components, such as `RELXILL` (Dauser *et al.* 2014) because disk reflection has been found only for a small fraction of AGN, all of them in the high accretion regime (Esparza-Arredondo *et al.* 2021). Finally, this spectral analysis lacks the inclusion of the Compton scattering, which contributes specially for Compton-thick⁷ (CT) sources. However, the available models within `XSPEC` (e.g., `CABS`) do not properly account for it as they assume an inadequate cross-section in the modelling (cf., Murphy and Yaqoob 2009, and `MYTORUS` manual⁸). Indeed, we also try the scenario in which `CABS` is included but we find the intrinsic luminosity to be unrealistically high in some cases (see Appendix A). Note that the exclusion of such a component leads to a systematic uncertainty, which is translated

⁵ The *NuSTAR* spectral resolution is 400 eV at 6 keV, see https://heasarc.gsfc.nasa.gov/docs/nustar/nustar_tech_desc.html

⁶ <https://ned.ipac.caltech.edu>

⁷ https://ned.ipac.caltech.edu/level5/March04/Comastri/Comastri_contents.html

⁸ <http://mytorus.com>

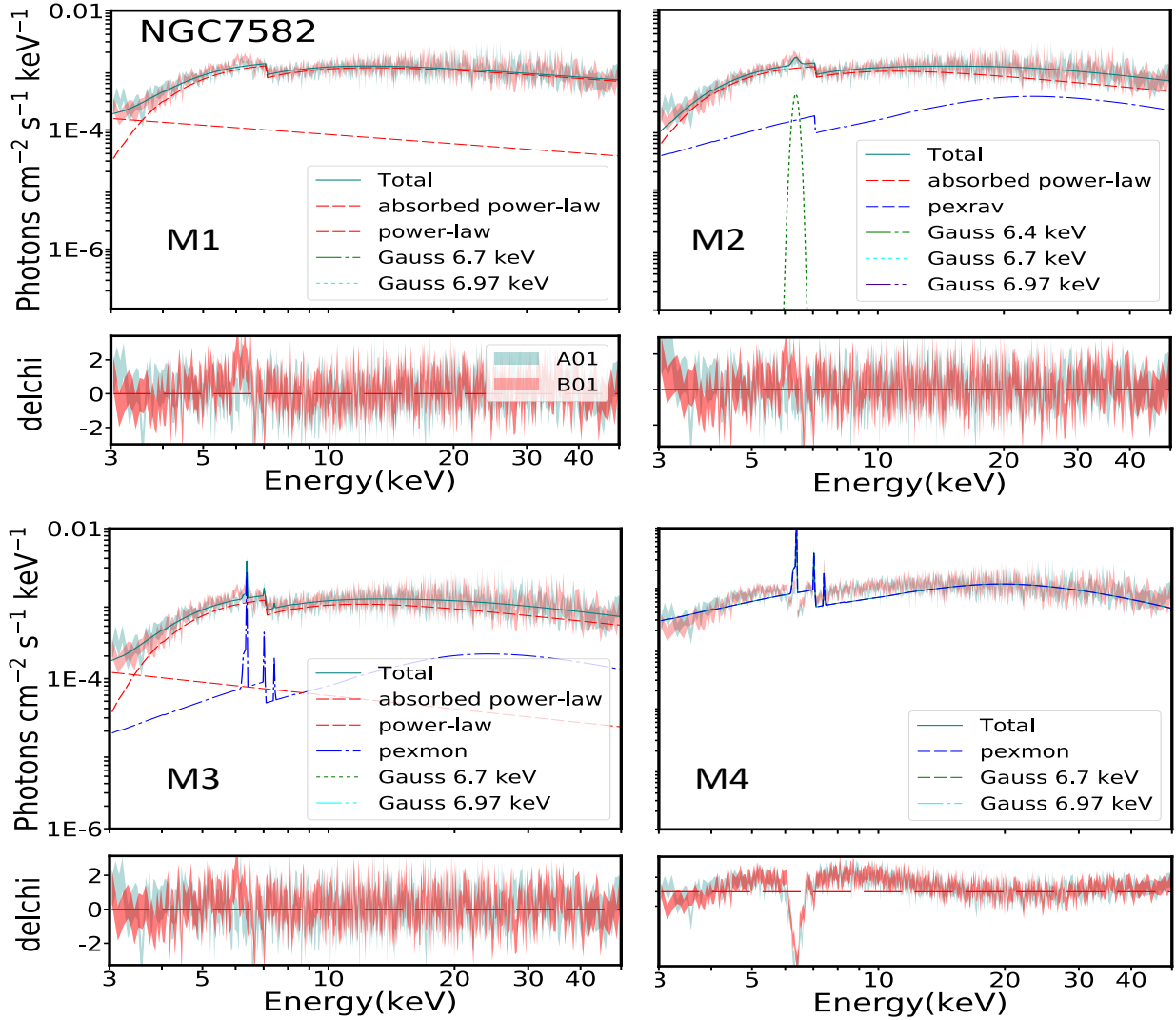


Figure 2. Spectral fits for M_1 (upper left), M_2 (upper right), M_3 (lower left) and M_4 (lower right) for NGC7582. Each color represents each of the components as follows: teal is the total spectrum, red is the partial-covering component, blue are pexmon (left) and pexrav (right) components, while green, cyan and purple are the extra lines in each model version. (see section 3.2)

into an underestimation of the intrinsic luminosities of CT sources. However, our baseline model has been widely used in several works aimed to find general properties of AGN and characterize the reflection component, even in CT objects (e.g., Kawamuro *et al.* 2016; Panagiotou and Walter 2019, 2020; Kang, Wang, and Kang 2020). Thus, the baseline model used in this work will lead to robust results that can be easily compared with previous works (e.g., Kawamuro *et al.* 2016; Annuar *et al.* 2015, 2017, 2020).

3.2 Spectral fitting

We start the analysis by fitting the spectra to M_1 . We then fit the spectra to M_2 , and obtain the EW and the luminosity of the $\text{FeK}\alpha$ line as explained above. We then fit the spectra to M_3 and test if reflection is required by the data using the f-test tool within `xSPEC`. If the f-test throws a probability value below 10^{-3} , then the reflection component is required by the data. For those objects for which the reflection component is required, we also test the statistical need for a power-law (i.e., we fit the spectra to M_4). Objects for which such

component is not statistically needed will be referred as reflection dominated.

We also estimate the reflection fraction, defined in this work as $C_{\text{ref}} = L_{\text{ref}}/L_{\text{cont}}$, where L_{ref} is the luminosity of the reflection component and L_{cont} is the luminosity of the intrinsic continuum, modelled with a power-law, with both luminosities calculated in the 3–70 keV energy range. They are computed using the `CLUMINOSITY` command within `xSPEC`. We estimate the $1-\sigma$ errors for the best-fit parameters. Errors in the luminosities of the different components, as well as in the EW of the $\text{FeK}\alpha$ line are presented as follows: if the $3-\sigma$ errors are well constrained, we present the $1-\sigma$ error; upper/lower limits correspond to the $3-\sigma$ estimates otherwise. This makes the analysis more conservative on the luminosity limit of the reflection component and the $\text{FeK}\alpha$ line for those sources where the reflection component or the $\text{FeK}\alpha$ line are not recovered by the data since it gives 99.6% the upper limit of the distribution. As for the reflection fraction, we perform MCMC simulations to recover its value and error as follows: we choose a random number within a normal distribution centered at the actual value whenever the lumi-

nosity is well constrained. However, when there is an upper/lower limit of the luminosity, we choose a random number drawn from a uniform distribution with limits zero and the upper/lower limit. We then calculate the ratio and repeat the same procedure 1000 times. Finally, we obtain the median for the central value and the 25th and 75th quartiles as the error range. Whenever the upper limit is above 1 or the lower limit is below 0, we report the value as a lower or upper limit, respectively.

Fig. 2 shows the best fit for M_1 (upper left), M_2 (upper right), M_3 (lower left) and M_4 (lower right) for NGC 7582 as an example of the resulting spectral fits. For this particular object, we obtain for M_1 a $\chi^2/\text{dof} = 699/675$, M_2 a $\chi^2/\text{dof} = 655/674$ for while for M_3 we obtain $\chi^2/\text{dof} = 650/674$, for which the f-test gives a value of 10^{-12} . Indeed, in the upper left panel of the figure, it is possible to see the poor fit and large residuals in particular around the $\text{FeK}\alpha$ line, indicating the need of an extra component to fit the spectrum. Also note that although upper right and lower left panels show different models, they both fit the data well, by accounting for the reflection component, mostly noticeable through the $\text{FeK}\alpha$ line. On the other hand, M_4 fits the data poorly with a $\chi^2/\text{dof} = 3115.7/677$ (see lower right panel). Indeed, although required, the line accounts only for $\sim 0.9\%$ of the reflection component, while the latter only accounts for $\sim 20\%$ of the 3-70 keV primary continuum luminosity. This is an example where the existence of the $\text{FeK}\alpha$ emission line, the f-test when comparing with the partial-covering intrinsic continuum model, and the luminosity detection limit, point out to the existence of a reflection component for this source.

4 RESULTS

Tables 3 and 4 present the best-fit parameters for both the LINER and Seyfert samples when fitted to the M_3 model. Note that we present the best-fit values for this model only as the analysis is based on this model version (see above). Note that for the covering factor, f_{cov} , we also test whether is zero or free to vary. In the cases in which it is zero, the source is not covered, corresponding to unobscured/low-obscured sources or, on the contrary, it is reflection dominated, thus the partially-covered continuum is not restricted. We mark the column with a dash line in these cases (six sources). However, although left free to vary, in many cases it is pegged to one (42 sources), indicating full covering of the source. As for the f-test, we conclude that when it is below 10^{-3} , the reflection component is statistically significant and is marked with the check mark symbol in this Col.(12). Among the 81 objects, we find that only NGC 424 is reflection dominated, i.e., the data do not require the addition of a power-law and the luminosity of this component is not restricted. This object is marked with an R in the Col. (1) of Table 4. The N_{H} cannot be calculated for this source. Moreover, we also find 18 other sources for which the f-test comparing models M_3 and M_4 does not favour the addition of a power-law component, although their N_{H} are well constrained. These objects have a large contribution of the reflection component in the CT regime, although the power-law continuum is still reachable thanks to the wide spectral range of *NuSTAR* data. As for intrinsic luminosities, as it was previously mentioned in section 3.2, these may be larger for CT objects as we are inducing a systematic uncertainty by excluding the Compton-scattering effect. Thus, we warn the reader that intrinsic luminosities reported here for CT objects should be treated a lower limits, even if they are well constrained by the spectral fits.

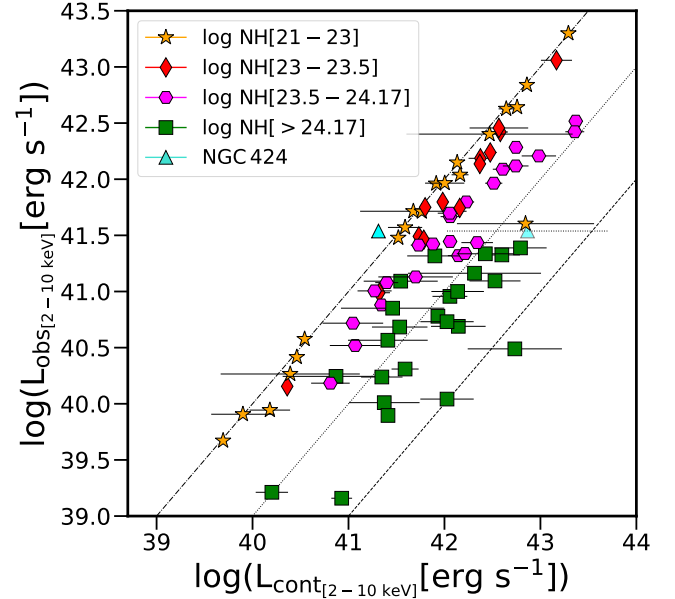


Figure 3. Observed 2-10 keV luminosity versus the intrinsic 2-10 keV luminosity. Note that the upper limits refer to the reflection dominated objects (see text). The dash-dotted, dotted, and dashed lines represent the 1:1, 1:10, 1:100 relations, respectively, indicating the correction factor that should be applied in order to obtain the intrinsic continuum luminosity from the observed luminosity. Orange stars, red diamonds, magenta hexagons and green squares are the N_{H} ranges shown in the figure label, while the cyan triangles are NGC 424 uncorrected (solid) and corrected (semi-transparent, see text).

4.1 Luminosity Correction

As mentioned in Section 2 we select sources with Eddington rate $L_{\text{bol,obs}}/L_{\text{Edd}} < 10^{-3}$ to study inefficient AGN with the public data available. However, we use as a proxy of the bolometric luminosity, the observed 2-10 keV X-ray luminosity (i.e. uncorrected from N_{H}). Indeed, the intrinsic luminosity and therefore the Eddington rate are expected to increase once we take into account the N_{H} . Fig. 3 shows the observed versus intrinsic 2-10 keV luminosity, the latter corrected from line-of-sight (LOS) obscuration according to the best fit reported in Tables 3 and 4.

The largest shift from the 1:1 relation is found for CT objects (green squares in Fig. 3), for which the luminosity can change more than a factor of ten. Note that NGC 424, classified as reflection dominated has long been studied at X-rays (e.g., Baloković *et al.* 2014; Hernández-García *et al.* 2015; Ricci *et al.* 2017; Marchesi *et al.* 2018), finding that this object has a large contribution of the reflection component, with weak signatures of the intrinsic continuum.

However, since we are unable to account for such a component, we calculate the bolometric luminosity through the luminosity of the reflection component as follows: we assume that the correction in the intrinsic luminosity for a certain object is given in the following form: $\log(L_{\text{cont}}) = A + \log(L_{\text{refl}})$, where A can be calculated through those CT objects for which the power-law is still detected in the spectra.

Moreover, by calculating the constant A for these objects, we can estimate how much the intrinsic luminosity changes for a certain amount of reflection. In practice, we estimate this factor using the green objects in Fig. 3 (i.e. 25 CT AGN). We find for our sample that $A = 1.5 \pm 0.8$. We then use this value to estimate the intrinsic luminosity for NGC 424. This extrapolation can be seen as the semi-transparent cyan triangle in Fig. 3.

Name	χ^2/dof	log NH	f_{cov}	Γ	EW	C_{ref}	log L _{(2–10) keV}		log L _{(3–70) keV}		f-test
(1)	(2)	(3)	(4)	(5)	(6)	(7)	continuum erg s ⁻¹	reflected erg s ⁻¹	continuum erg s ⁻¹	reflected erg s ⁻¹	(12)
		cm ⁻²			eV		(8)	(9)	(10)	(11)	
NGC1052	744.71/734	23.15 ^{+0.03} _{-0.03}	1*	1.78 ^{+0.04} _{-0.04}	139.30 ± 27.4	0.15 ^{+0.06} _{-0.06}	41.73 ± 0.01	40.21 ± 0.15	42.14 ± 0.01	41.32 ± 0.15	✓
NGC2655	84.87/94	23.41 ^{+0.12} _{-0.12}	1*	2.05 ^{+0.17} _{-0.15}	368.43 ± 105.	0.56 ^{+0.35} _{-0.26}	41.32 ± 0.10	40.30 ± 0.17	41.59 ± 0.07	41.23 ± 0.17	x
UGC5101	54.98/47	23.84 ^{+0.06} _{-0.06}	1*	< 1.26	< 451.	< 1	42.61 ± 0.09	< 41.7	43.45 ± 0.08	< 43.4	x
M81	1372.00/1246	22.16 ^{+0.13} _{-0.09}	-	1.94 ^{+0.01} _{-0.01}	33.78 ± 9.45	< 0.024	40.54 ± 0.01	< 38.2	40.88 ± 0.15	< 39.2	x
NGC3079 ^{CT}	114.37/123	24.41 ^{+0.05} _{-0.05}	0.98 ^{+0.01} _{-0.01}	1.68 ^{+0.16} _{-0.15}	479.64 ± 210.	0.10 ^{+0.06} _{-0.05}	41.59 ± 0.13	39.83 ± 0.20	42.06 ± 0.05	41.01 ± 0.20	✓
UGC5881	136.07/163	23.43 ^{+0.21} _{-0.36}	0.52 ^{+0.19} _{-0.25}	1.75 ^{+0.16} _{-0.16}	215.40 ± 75.1	0.37 ^{+0.37} _{-0.26}	42.37 ± 0.11	41.18 ± 0.33	42.80 ± 0.07	42.31 ± 0.33	x
NGC3628	64.43/81	< 22.07	-	2.05 ^{+0.09} _{-0.09}	< 100.	< 0.230	40.18 ± 0.20	< 38.4	40.32 ± 0.27	< 39.3	x
NGC3718	192.45/202	23.79 ^{+0.13} _{-0.13}	< 0.06	2.21 ^{+0.06} _{-0.04}	< 91.1	< 0.111	41.07 ± 0.25	< 39.1	41.43 ± 0.27	< 40.1	x
NGC3998	613.34/709	22.36 ^{+0.74} _{-0.49}	-	1.98 ^{+0.04} _{-0.03}	< 18.4	0.05 ^{+0.07} _{-0.03}	41.59 ± 0.17	39.76 ± 0.27	41.89 ± 0.16	40.73 ± 0.27	x
NGC4102	181.53/194	23.68 ^{+0.06} _{-0.07}	1*	1.26 ^{+0.11} _{-0.11}	< 312.	0.29 ^{+0.22} _{-0.18}	41.34 ± 0.06	40.00 ± 0.27	42.08 ± 0.04	41.50 ± 0.27	x
M106	431.61/460	23.02 ^{+0.15} _{-0.03}	> 0.87	1.86 ^{+0.07} _{-0.04}	< 112.	< 0.151	40.36 ± 0.03	< 38.8	40.73 ± 0.03	< 39.8	x
M58	802.22/732	22.34 ^{+0.09} _{-0.11}	1*	2.01 ^{+0.04} _{-0.04}	120.73 ± 21.4	0.08 ^{+0.05} _{-0.05}	41.52 ± 0.01	39.75 ± 0.27	41.81 ± 0.01	40.70 ± 0.27	x
NGC5005	26.45/34	22.96 ^{+0.39} _{-0.48}	0.68 ^{+0.32} _{-0.01}	> 2.37	348.49 ± 145.	> 0.05	40.39 ± 0.71	39.58 ± 0.20	40.50 ± 0.61	40.25 ± 0.20	x
NGC6240	374.82/439	24.12 ^{+0.03} _{-0.03}	0.95 ^{+0.01} _{-0.01}	1.63 ^{+0.07} _{-0.07}	398.33 ± 74.3	0.17 ^{+0.06} _{-0.05}	43.37 ± 0.06	41.87 ± 0.12	43.87 ± 0.02	43.08 ± 0.12	✓
MCG+08-31-041	200.10/241	< 22.47	> 0.21	1.96 ^{+0.09} _{-0.08}	150.75 ± 63.9	0.42 ^{+0.25} _{-0.20}	42.64 ± 0.07	41.52 ± 0.20	42.90 ± 0.04	42.51 ± 0.20	✓
NGC7130 ^{CT}	43.65/58	24.27 ^{+0.16} _{-0.25}	1*	< 1.50	715.41 ± 213.	> 0.42	41.54 ± 0.38	40.92 ± 0.26	42.29 ± 0.19	42.44 ± 0.26	✓
NGC7331	133.31/147	22.39 ^{+0.27} _{-0.43}	1*	2.13 ^{+0.16} _{-0.05}	< 182.	< 0.437	40.46 ± 0.04	< 39.4	40.69 ± 0.03	< 40.2	x
NGC7479 ^{CT}	71.56/78	24.78 ^{+0.05} _{-0.06}	1*	1.86 ^{+0.61} _{-0.34}	693.07 ± 246.	0.20 ^{+0.45} _{-0.17}	42.73 ± 0.48	40.45 ± 0.48	42.80 ± 0.24	41.51 ± 0.48	✓

Table 3. Spectral fit results for the LINER sample. Column(1) is the name of the source, (2) is the χ^2/dof , where dof are the degrees of freedom. Columns (3)-(7) are the column density, log NH in units of cm⁻², the covering factor, the photon index, Γ , the equivalent width (EW) in units of eV and the reflection fraction respectively, while columns (8)-(11) are the continuum and reflected luminosities in units of erg s⁻¹, in the (2-10 keV) and (3-70 keV) bands, respectively. Column (12) is the f-test performed between models 1 and 3 in all cases. The checkmark (✓) symbol represents a f-test <1E-4, while the x symbol represents otherwise. In Col. (1), the superscript RD is for reflection-dominated sources, while those marked with CT are the Compton-thick sources in our sample, whereas in Col. (4) the dash means that the covering factor is zero, therefore no emission is scattered, and the * symbol means that the parameter is frozen.

Fig. 4 shows the final distribution for the Eddington rate in our sample when the obscuration is properly taken into account, compared to the initial Eddington rate, estimated through the observed X-ray luminosity. Indeed, a shift towards greater Eddington rates is seen in objects with larger N_{H} (mostly CT objects) and a decrease in objects with lower Eddington rates. The mean Eddington rate of the sample is $\langle \log(\lambda_{\text{Edd}}) \rangle = -3.3$ (dash-dotted vertical line in Fig. 4) with a 1σ range of $[-5.2, -1.49]$ (see dotted lines in the figure), roughly expanding four orders of magnitude in Eddington rate. Additionally, the lack of Compton-scattering may shift CT objects to even higher Eddington rates (as intrinsic luminosities may be even larger). As it was previously mentioned in section 2.2, we are aware that our selection criteria bias our sample towards a large LOS obscuration for Eddington rate between $-2.5 < \log \lambda_{\text{Edd}} < -1.49$ (14 CT AGN). Thus, we will exclude these sources from the discussion as we are missing an important portion of objects residing in this range of Eddington rates (mostly highly obscured objects with intrinsically higher Eddington rates). Moreover, the discussion will be based on the remaining 67 sources.

4.2 Existence of the reflection component

We base our analysis on the existence of the reflection component in three criteria: (1) the detection of the FeK α line; (2) a statistical significance of the reflection component compared to the model without reflection (i.e. f-test < 0.001 when comparing models M₁ and M₃), and (3) the restriction of the reflection luminosity at $3-\sigma$.

We detect the FeK α emission line in 61 out of the 81 sources (~ 75% of the sample). On the other hand, the inclusion of a reflection component improves the spectral fit for 46 out of the 81 sources (~ 57% of the sample). Additionally, we restrict the luminosity of the reflection component for 67 out of the 81 sources (i.e. ~ 83%). A total of 45 out of 81 (~ 55%) sources fulfill the three criteria to establish the existence of the reflection component, while 15 (~ 19%) meet two out of the three criteria, and 9 (~ 10%) meet only one of the criteria

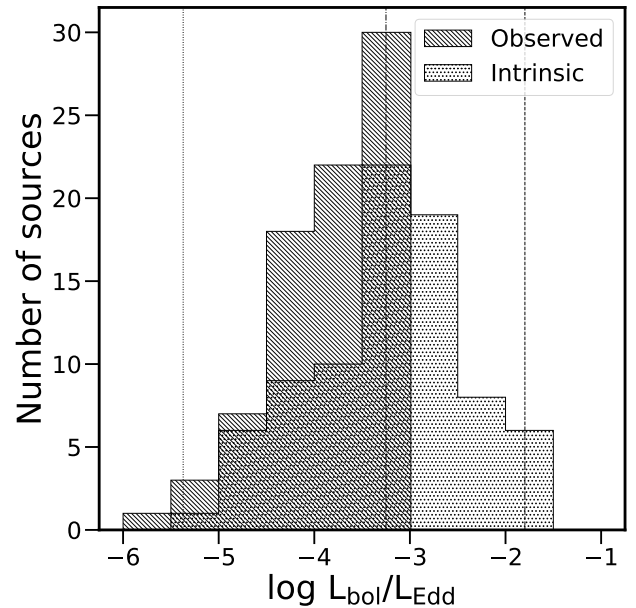


Figure 4. Comparison between the Eddington rate obtained with a rough fit to a simple power-law (dashed histogram) versus the Eddington rate obtained once a proper obscuration is accounted for (dotted histogram).

(namely M 81, NGC 3998, NGC 4102, NGC 253, 2MXJ 0114-5523, UGC 3601, 2MXJ 0756-4137, IC 751, and Mrk 231).

As for the 15 sources fulfilling two criteria, one (Mrk 1066) statistically needs the reflection component and it is well constrained. However, the FeK α emission line is not well detected at a $3-\sigma$ limit. Note that the spectrum is a low-quality spectrum (dof < 50) which may cause a poor restriction of the three lines at 6.4, 6.7 and 6.97 keV. In order to test this possibility, we use the non-grouped spectrum of the source and check which line is present. Indeed, the line present in this

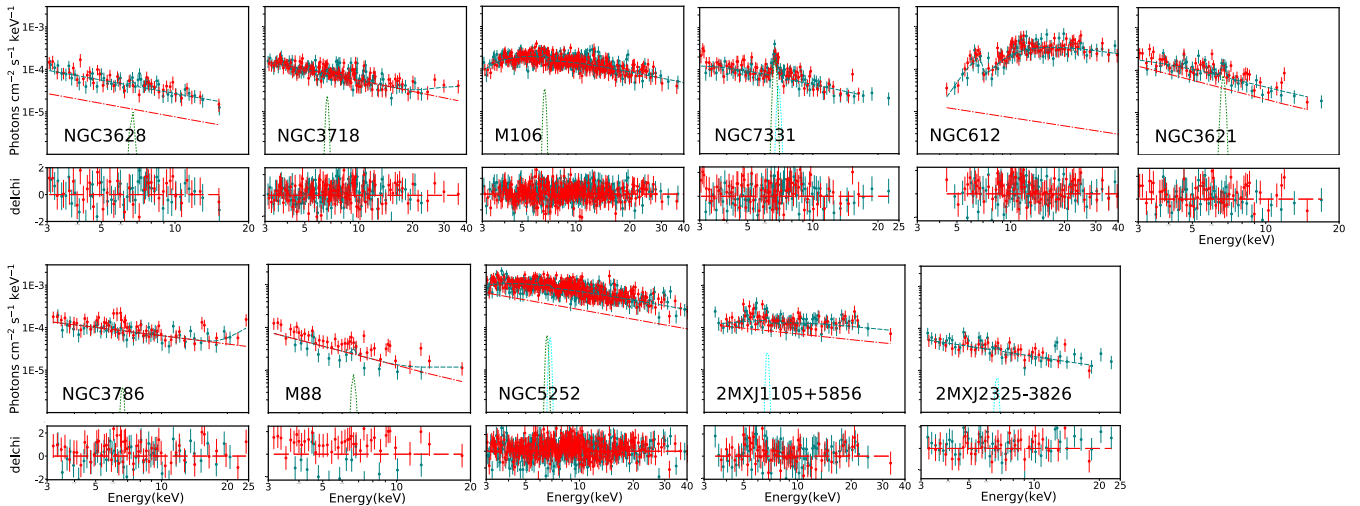


Figure 5. Spectral fits for our eleven candidates for the disappearance of the torus. Colors and axis labels are as in Fig. 2. Note that we have ionized lines are present in all the objects (except for NGC 612) and that we have tested the scenario in which the FeK α line could be the responsible for the line feature, finding that such line is not present in any of the spectra. Also note that for M 88 both FPMA and FPMB modules seem to be misaligned with a normalization factor of 1.99, well above the overall sample.

object is the FeK α emission line. Once we remove both ionized lines from the fit, and calculate the EW and flux for the FeK α emission line for this source, we obtain a constrained parameter. Thus, we can safely say that this source fulfills the three criteria.

The remaining 14 objects, with two out of the three criteria, fulfill the detection of the FeK α emission line and a constrained luminosity for the reflection component. However, statistically speaking, the reflection component is not needed. Among them, all but NGC 5695 show a relatively low reflection fraction (C_{ref}) and/or N_{H} . Thus, the reflection component is present mainly through the FeK α emission line while the Compton hump is suppressed under the intrinsic continuum. Under this scenario, the f-statistic is not suitable to test the presence of the reflection component because it only affects a narrow range of the spectrum where the FeK α emission line is located. In the case of NGC 5695, it shows a relatively high N_{H} . In this case, the quality of the spectrum for this source might be responsible for the statistical significance of the reflection component.

As for the objects fulfilling only one criterion, seven objects (NGC 3998, NGC 4102, 2MXJ 0114-5523, UGC 3601, 2MXJ 0756-4137, IC 751 and Mrk 231) meet the restriction of the luminosity of the reflection component, and the remaining two objects (M 81 and NGC 253) meet the detection of the FeK α emission line. The detection of the reflection component without the FeK α line can be due to a combination of high absorption which can lead to the detection of a Compton hump and a low S/N spectrum which can lead to the poor restriction of the line. The detection of the FeK α line without statistical significance for the reflection component can again be explained due to low N_{H} and/or low reflection fraction as indicated above. Moreover, the non-detection of the Compton hump may also depend on the shape of the spectrum; for highly obscured sources it may only require data up to 10 keV, while for low obscured sources, the Compton hump requires high S/N up to 30 keV.

We find that 12 objects do not present any signs of reflection (namely UGC 5101, NGC 3628, NGC 3718, M 106, NGC 7331, NGC 612, 2MXJ 1105+5856, NGC 3621, NGC 3786, M 88, NGC 5252 and 2MXJ 2325-3826). Note that five out of these 12 objects are LINERs while the remaining seven are Seyferts. How-

ever, several works have found traces for the reflection component in UGC 5101 (e.g., González-Martín *et al.* 2009; Oda *et al.* 2017; La Caria *et al.* 2019). In addition, the fact that the spectrum has a low S/N leads us to exclude it from our final sample of candidates for the disappearance of the torus. Fig. 5 shows the spectral fits for our final sample of 11 candidates to the torus disappearance ($\sim 12\%$). All but NGC 612 can be modelled with a single power-law⁹ with little obscuration, supporting the idea that the reflection component is not present in these objects.

Altogether, we present 11 candidates which lack the reflection component, related to the plausible disappearance of the torus using X-rays observations. Among them, we find that eight sources have studies aiming to find the reflection component or the torus (through X-rays/mid-IR). For all of them we find complete agreement with the idea of the absence of the reflection component associated with the torus in previous works (see Sec. 5).

4.3 Reflection strength

We explore here the degree of the reflection component strength for the objects in our sample. Fig. 6 shows the luminosity distribution for the intrinsic continuum (left histogram), FeK α emission line (upper right histogram) and reflection (right histogram). Note that for both the reflection and FeK α line distributions, we only show those sources for which the parameter is well constrained.

The FeK α line luminosity ranges from $\log(L_{6.4 \text{ keV}}) \sim [38. - 41.3]$, with a mean value of $\langle \log(L_{6.4 \text{ keV}}) \rangle = 40.1$, the reflection luminosity ranges from $\log(L_{\text{ref}(3-70 \text{ keV})}) \sim [37.5, 43.2]$, with a mean value of $\langle \log(L_{\text{ref}(3-70 \text{ keV})}) \rangle = 41.9$, and the intrinsic 3-70 keV luminosity ranges from $\log(L_{\text{cont}(3-70 \text{ keV})}) \sim [39.8, 43.9]$, with a mean value of $\langle \log(L_{\text{cont}(3-70 \text{ keV})}) \rangle = 42.3$ (see dashed lines in the histograms). Thus, all these three luminosities span around four orders of magnitude.

⁹ Note that all of them present ionized emission lines.

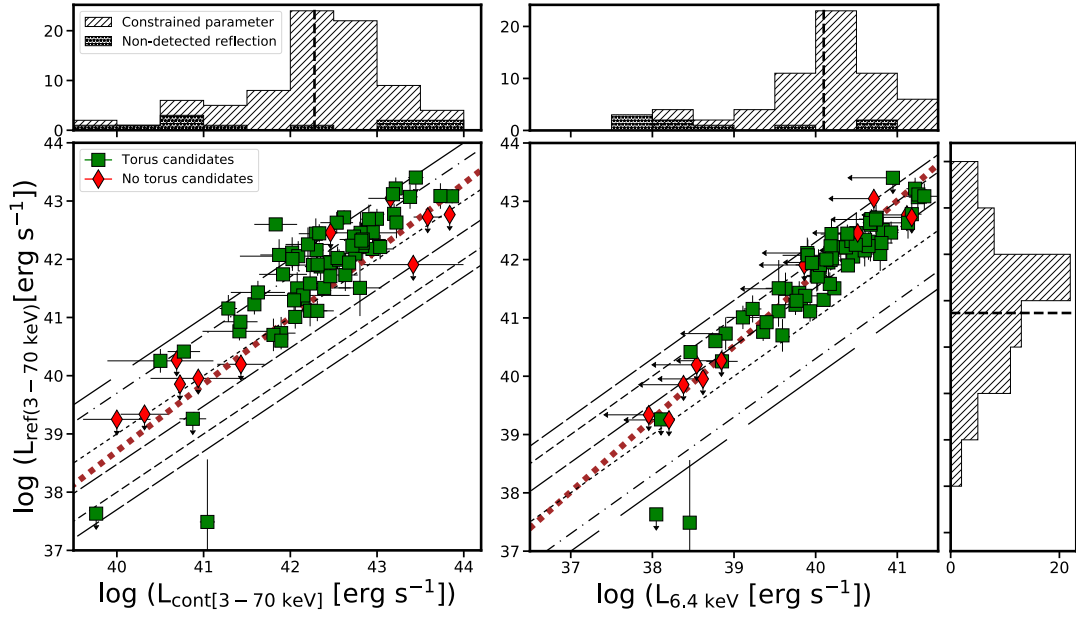


Figure 6. 3-70 keV band luminosity of the reflection component versus that of the intrinsic continuum (left) and the FeK α emission line luminosity versus the 3-70 keV reflection luminosity (right). In both cases, lines represent the percentage of the quantity in the Y axis with respect to the X axis. From top to bottom 100, 50, 10, 3, 1, and 0.5% of the intrinsic (large left panel) and reflection (large right panel) luminosities. The red diamond and green square are objects well fitted with the power-law components (i.e. no reflection candidates) and with the combination of reflection plus power-law components, respectively. The thick dotted brown line in both panels represent the linear correlation found for the quantities in each panel when the X axis is the independent quantity, while the black dashed line in the histograms represents the mean of each quantity. The histograms in the top and right panels are the distribution of the different luminosities (see text).

The reflection component represents, on average, 40% of the intrinsic continuum luminosity of the source, (i.e. $\langle C_{\text{ref}} \rangle = 0.41$ ¹⁰). In 20 out of the 81 sources the reflection is below 20% of the intrinsic continuum (i.e. $C_{\text{ref}} < 0.2$), 28 sources fall in the range $0.2 < C_{\text{ref}} < 0.6$, and 5 fall in the range $C_{\text{ref}} > 0.6$, while the remaining 28 sources have lower limits for C_{ref} . On the other hand, around 50% of the sample (41 sources) is located in the area where FeK α luminosity accounts for 1-3% of the reflection component luminosity, 15% (12 sources) is consistent with 3-10%, and 6% (five sources) sources present a weak line luminosity, accounting for less than 1% of the reflection component. As for the remaining 28% (23 sources), either the EW of the FeK α line and/or the luminosity of the reflection component are upper limits, therefore the fraction is an upper limit as well. Naturally, the 11 candidates lacking of reflection signatures are included in this group.

In order to study the connection between these luminosities, the large panels in Fig. 6 show the correlation between the reflection luminosity versus the intrinsic continuum (left panel) and the FeK α emission line (right panel) luminosities. As expected, the three quantities are well correlated. Moreover, the reflection component and the FeK α emission line are slightly better correlated (with a Pearson’s coefficient of 0.93) than the intrinsic continuum and the reflection component (with a Pearson’s coefficient of 0.89).

In order to obtain the best characterization of the relation between those parameters, we use a bootstrap method to account for possible outliers in the correlations, by choosing a random subsample with 80% of the total sample and repeating this process a total of 100 times. For each random subsample, we also perform a MCMC sim-

ulation similar to that mentioned in section 3.2: for each luminosity pair, we choose a random number drawn from a normal distribution whenever the value is well constrained, and from an uniform distribution whenever there are upper/lower limits involved. We then perform a binning method in the x axis by dividing it into bins of $dx = 0.5$ dex, and obtain the median and standard deviation along both axes. We calculate the correlation through a linear regression method and obtain the slope, intercept, and the r - and p -values. We repeat this process 100 times and then estimate the mean values of all quantities. As for the correlation between L_{ref} and $L_{6.4 \text{ keV}}$ we also perform the linear regression analysis assuming that the luminosity of the reflection component is the independent component and the luminosity of the line is the dependent one. We present the best correlation found after performing a bisection method from both correlations. In this case the fraction of the luminosity of the FeK α line over the Compton hump increases from 1% at $\log(L_{\text{ref}}) = 43$ to $\sim 5\%$ at $\log(L_{\text{ref}}) = 40$ and to $\sim 10\%$ at $\log(L_{\text{ref}}) = 38$. Both correlations can be represented in the following form (represented as the thick dotted brown lines in Fig. 6):

$$\log(L_{\text{ref}}) = (1.13 \pm 0.22) \log(L_{\text{cont}}) - (6.43 \pm 9.35) \quad (6)$$

$$\log(L_{\text{ref}}) = (1.24 \pm 0.15) \log(L_{6.4 \text{ keV}}) - (8.17 \pm 6.16) \quad (7)$$

Note that we also explore if this trend is seen over the intrinsic continuum or the Eddington rate but no correlation is found.

4.4 Obscuration

The LOS obscuration and the reflection might occur in the same structure (i.e., the torus), thus both the reflection and the obscuration may be related. Therefore, a proper estimate on the N_{H} is necessary

¹⁰ Note that this value is calculated for objects with both luminosities well constrained (i.e., neglecting upper/lower limits.)

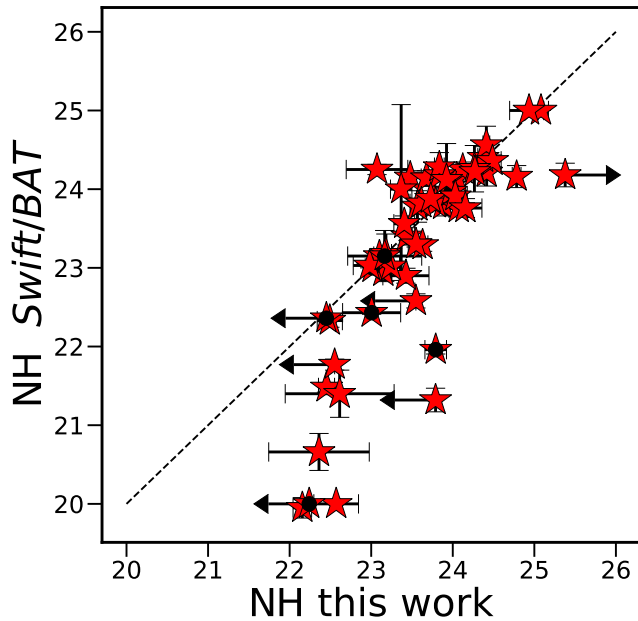


Figure 7. Comparison between our N_{H} estimates and the values reported in Ricci *et al.* (2017) for the common sample. Sources with a black dot inside the red star are the candidates for the torus disappearance in our sample. Note that upper limits in our analysis might be due to the fact that the sources are low-obscured or unobscured (see text).

in order to place solid conclusions on the reflection component. For this purpose, Fig. 7 shows the comparison between the N_{H} found in this analysis compared to those presented in Ricci *et al.* (2017). They analyze the X-ray properties of the *Swift*/BAT sample for which we find 53 sources in common. We find that for most sources, the LOS obscuration found in both works are well in agreement when their column density is $N_{\text{H}} > 3 \times 10^{22} \text{cm}^{-2}$. We find discrepancies for seven objects below $N_{\text{H}} < 3 \times 10^{22} \text{cm}^{-2}$, which may be expected since *NuSTAR* does not cover energies below 3 keV, necessary to constrain low values of obscuration. Moreover, Fig. 8 (right histogram) shows the N_{H} distribution for our sample. We find a mean column density of $\langle \log(N_{\text{H}}) \rangle = 23.74$ (see dashed line in the figure). We also find that 24 sources are CT AGN (i.e., $\log N_{\text{H}} > 24.17 \text{cm}^{-2}$) while 45 out of the 81 are Compton-thin and 12 are unobscured sources. In addition, the majority of sources with no clear indication of reflection appear to be below the CT regime. On the other hand, the EW of the FeK α line shows a mean value of $\langle \log(\text{EW}(\text{FeK}\alpha)) \rangle = 2.89$ (Fig. 8, top histogram), with 20 sources presenting upper limits. Using *Suzaku* and *Swift*/BAT data, Kawamuro *et al.* (2016) also study a sample of 10 inefficient AGN. Among the seven objects in common with our sample, three (NGC 3718, NGC 4941 and NGC 5643) show different values for N_{H} (discrepancies around 10-20%). We find higher N_{H} for the three sources, even when accounting for error bars. However, note that although the model is quite similar, they allow the reflection fraction in pexrav and the constant (which they relate to the scattering fraction) free to vary in all cases. The main difference is that we test whether letting the covering fraction free to vary significantly improves the fit. This might explain the N_{H} differences found in both analyses.

Marchesi *et al.* (2018) analyze a sample of 26 sources classified as CT, using *NuSTAR* along with other X-ray facilities. Among those objects, we find 14 sources in common with our work, from which 10 have similar value of N_{H} compared to ours, while three have

small discrepancies on the N_{H} (i.e. lower than 10%), and one case (NGC 424) for which we have strong differences: they report a reflection dominated source, with $N_{\text{H}} = 24.4$, while from our analysis it should be considered as highly obscured ($\log(N_{\text{H}}) = 23.1$). Indeed, this source is also reflection dominated according to our f-test analysis. Thus, statistically speaking, the obscured power-law associated with the intrinsic continuum is not required by the data. Moreover, their reflection model is different to ours, which might be responsible for the small changes in the spectral parameters.

Panagiotou and Walter (2019) also studied six sources in common with this work (M 106, NGC 1194, NGC 4941, NGC 5643, NGC 5728, and NGC 7582). All but two (NGC 4941 (24.09 ± 0.15) and NGC 1194 (23.7 ± 0.1)) present consistent N_{H} values. NGC 4941 and NGC 1194 present higher N_{H} compared to ours, even when accounting for error bars. Again, they classify these two sources as reflection dominated so this might be affecting the constraint of the LOS absorption due to a weak detection of the intrinsic continuum. In a second paper of the series, Panagiotou and Walter (2020) include *NuSTAR* data for other six sources in common with our analysis (NGC 1052, NGC 2655, M 106, NGC 5252, NGC 5283 and NGC 7213), also showing consistent N_{H} . Note that Panagiotou and Walter (2020) exclude in their sample selection 21 sources in common with our sample; four (M 81, NGC 3998, NGC 7130, and NGC 7479) are excluded due to their LINER nature, two (IC 751 and NGC 7582) due to variability, and the remaining 15 are excluded for being reflection dominated (although included in Panagiotou and Walter 2019).

We plot the expected correlation between the N_{H} and the EW(FeK α) emission line in the large panel of Fig. 8. The equivalent width increases when the N_{H} does so, with a Pearson's linear relation coefficient of 0.85 (linear fit shown as dotted brown line in the figure). This is well explained by the predicted EW from a uniform shell of material encompassing the continuum source (blue long-dashed line in large panel of Fig. 8, see also Fig. 2 in Leahy and Creighton 1993). Moreover, Guainazzi, Matt, and Perola (2005) propose a slight change in this correlation when the reflection occurs in the inner walls of an optically-thick matter, as seen through the unobscured LOS, while the continuum is obscured by material along the LOS (see pink dashed line in Fig. 8 and Fig. 9 in Guainazzi, Matt, and Perola 2005). Note that the dispersion on this relation is naturally explained through the differences in geometry and composition of the reflector. Therefore, this reinforces the good estimate on the N_{H} in our analysis. This is also reproduced in more recent models with spherical and torus-like geometries (e.g Ikeda, Awaki, and Terashima 2009; Tanimoto *et al.* 2019). Moreover, we explore how the EW is affected by the amount of obscuration and the strength of the line (see shaded area in Fig. 8). We choose NGC 1052 as a test object and vary the normalization of the FeK α line (from $\text{norm}_{6.4\text{keV}} = 0.5$ to $\text{norm}_{6.4\text{keV}} = 5$), from left to right, respectively, while changing the N_{H} in order to see how the relation should change. We find that there is a value of EW above which this correlation saturates and thus we would only measure reflection (i.e., in the cases of reflection dominated sources). The main reason for the differences between this work and Guainazzi, Matt, and Perola (2005) is the fact that they do not have very obscured sources in their sample and thus their best fit does not cover such range. Thus, we confirm that 69 out of the 81 objects ($\sim 85\%$) are obscured at X-rays (i.e. $N_{\text{H}} > 3 \times 10^{22} \text{cm}^{-2}$). This is further discussed in Section 5.

Furthermore, more than half of the sources (42) appear to be completely covered, 27 present a covering factor $f_{\text{cov}} > 0.5$, while seven show $f_{\text{cov}} < 0.5$. The remaining five AGN present either upper limits or non-constrained estimates for the covering factor. Among these

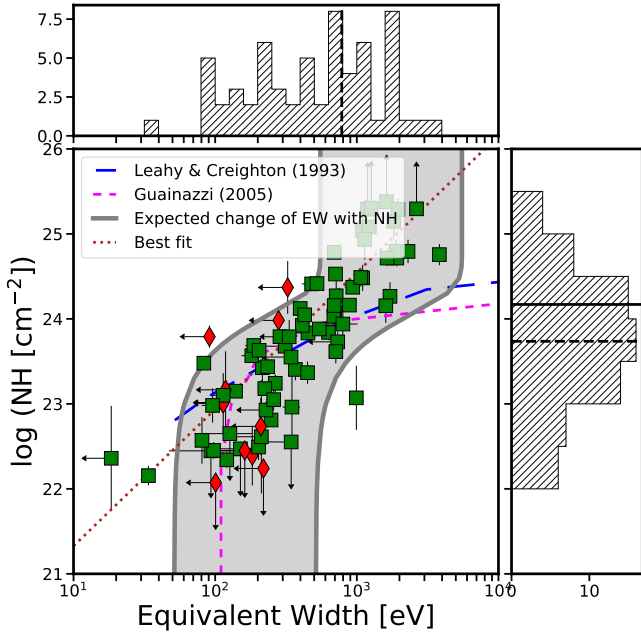


Figure 8. Equivalent width of the FeK α line versus the column density along the LOS. Colors and symbols are as in Fig. 6. The correlation line is drawn as the brown dotted line while the blue long-dashed line and pink dashed lines show the expected relation according to Leahy and Creighton (1993) and Guainazzi, Matt, and Perola (2005), respectively. Moreover, the gray shaded area corresponds to the case in which the EW changes according to different levels of obscuration and reflection (see text).

objects, all of them present either low N_{H} or upper limits whereas the sources presenting full covering, also present high obscuration (with only 6 sources being mildly obscured).

5 DISCUSSION

The aim of this work is to study the behaviour of the reflection component and obscuration at X-rays (classically associated with the torus) at low accretion rates. In order to trace such a component, we selected a sample of 81 sources with *NuSTAR* observations among all the nearby AGN observed so far with available M_{BH} measurements. We performed a spectral analysis with a model that accounts for the reflection component from neutral material plus a partially absorbed intrinsic continuum.

Early X-ray observations of local AGN have served as observational proofs of the AGN unified theories, showing that most type-1 AGN are unobscured while type-2 AGN tend to show obscuration exceeding $N_{\text{H}} > 10^{22} \text{cm}^{-2}$ (Awaki *et al.* 1991; Bassani *et al.* 1999). However, since then, several authors have shown that the fraction of obscured sources might depend on the evolutionary stage of the sources (see Ramos Almeida and Ricci 2017, for a review).

The covering factor of the gas can be estimated studying the absorption properties of large samples of AGN. In Fig. 9 we compare the results found by Ricci *et al.* (2017) using the BASS sample and those found in this study (numbers are reported in Table 5). Using this technique, recent hard X-ray studies have shown that the fraction of CT sources below $\lambda_{\text{Edd}} \sim 0.032$ is $23 \pm 6\%$ (blue shaded area in Fig. 9). Marchesi *et al.* (2018) find that the fraction of CT sources decreases when using *NuSTAR* data thanks to a better covering and

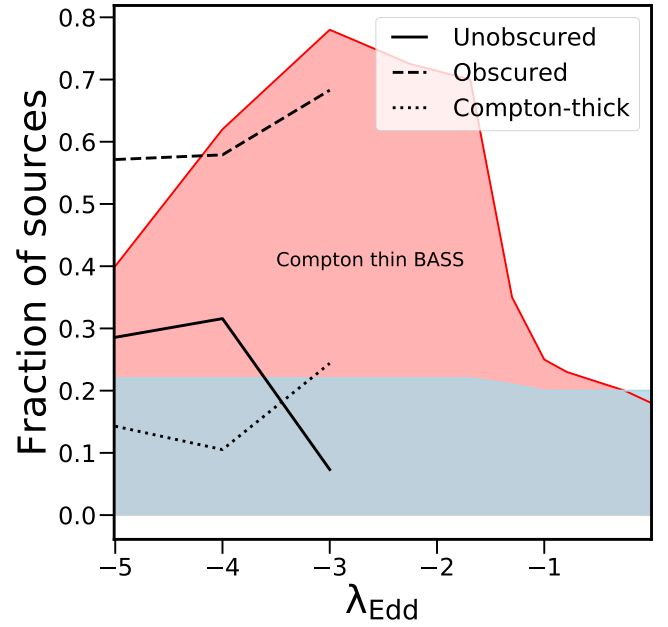


Figure 9. Fraction of Compton-thin and Compton-thick sources for the *Swift*/BAT sample reported by Ricci *et al.* (2017) (red and blue shaded areas, respectively) compared to the unobscured, obscured and CT (solid, dashed and dotted lines, respectively). Note that our sample is limited above $\lambda_{\text{Edd}} > -2.5$ due to the selection criteria we use in this work.

sensitivity above 10 keV which allows a better restriction in the LOS obscuration affecting the intrinsic continuum.

Our results indicate that the fraction of CT sources at $\lambda_{\text{Edd}} \approx 10^{-5}$ is 15% (dotted line), while Ricci *et al.* (2017) find it to be $\sim 20 \pm 4\%$. Thus, our results are statistically in agreement with them. Meanwhile, Ricci *et al.* (2017) find that the peak of obscured sources happens around $\lambda_{\text{Edd}} \sim 10^{-3}$, rising from 20% to 80% at Eddington rates $\lambda_{\text{Edd}} \approx 10^{-1}$ and $\lambda_{\text{Edd}} \approx 10^{-3}$, respectively (see red shaded area in Fig. 9, see also Ricci *et al.* 2017). Interestingly, our sample agrees well with these numbers at $\lambda_{\text{Edd}} \approx 10^{-3}$ for the percentage of obscured AGN (dashed line in Fig. 9). Note that our results indicate a low population of unobscured sources at $\lambda_{\text{Edd}} \approx 10^{-3}$. Moreover, a slight decrease on the fraction of Compton-thin obscured sources is found below $\lambda_{\text{Edd}} \approx 10^{-3}$, reaching $\sim 60\%$ at $\lambda_{\text{Edd}} \approx 10^{-5}$. Correspondingly, the fraction of unobscured sources rises from ~ 6 at $\lambda_{\text{Edd}} \approx 10^{-3}$ to $\sim 30\%$ at $\lambda_{\text{Edd}} \approx 10^{-5}$. Nonetheless, we are aware that this may be due to a bias in the selection criteria. Indeed, if there were more unobscured sources at these Eddington rates, they should have been included in our sample. However, we select only those sources with archival data and a minimum S/N in the spectrum. This has two main consequences: i) there may be several objects which have not yet been observed, among which there might be unobscured sources. ii) there might be more obscured sources for which the flux is so low that they do not fulfill our S/N criteria. Thus, although our results are in agreement with the complete sample by Ricci *et al.* (2017), we warn the reader that our sample is incomplete.

The trend found in this analysis might suggest no obscuration for a large fraction of sources at even lower accretion rates. The scenario in which both the BLR and the torus can be seen as different regions from a wind coming off the disk has long been proposed (Elvis 2000) and it naturally includes the absence of such regions in some objects (e.g., True-type 2 AGN intrinsically miss the BLR

Tran 2001; Laor 2003; Panessa *et al.* 2006). If the accretion disk cannot expel material in an efficient way, then the gravitational force from the SMBH will overcome the radiation pressure from the wind, causing the wind, and therefore the BLR and the torus, to collapse (Elitzur and Shlosman 2006). Therefore, as a first approach, the condition for the torus disappearance can be related to the bolometric luminosity of the source and the accretion rate. According to Elitzur and Shlosman (2006), the BLR should disappear for low-luminosity AGN (i.e., $L_{\text{bol}} < 10^{42} \text{ erg s}^{-1}$). Six out of the 11 objects lacking reflection signatures in our sample are below this threshold. However, in a more recent study it has been shown that this structure can disappear even for bright sources (e.g. Elitzur and Netzer 2016), depending on the properties of the wind, such as the wind efficiency or the number/density of clouds. In fact, it requires a minimal column density, implying a minimal outflow rate and thus a minimal accretion rate. Interestingly, three of our candidates present upper limits on the N_{H} and other five show $N_{\text{H}} \leq 10^{23} \text{ cm}^{-2}$. Finally, three are rather obscured (namely M 106, NGC 612 and M 88). In particular, for M 106, Kawamuro *et al.* (2016) find that the FeK α line is variable, proposing it might be originated in the accretion disk, while in the case of NGC 612, Ursini *et al.* (2018) do not find strong features of a Compton-reflection component, although like us, they find that this source presents high absorption, proposing that it might originate in an extended structure rather than the pc-scale torus. Thus, these works are still in agreement with the lack of reflection originated in the torus. Another particularly interesting object is M 88, being proposed as a True-Type 2 AGN (i.e., intrinsically missing the BLR, Brightman and Nandra 2008). We would expect for this object to be low-obscured. Although we modelled this source with an obscured component, the quality of the observations¹¹ may prevent us from finding a reliable value in the N_{H} for this particular source. Thus, almost all our candidates to the torus disappearance are on the lower end of LOS obscuration (Fig. 8).

According to Elitzur and Netzer (2016), the BLR/torus may or may not exist in a delimited zone in the luminosity- M_{BH} diagram and both components should disappear under a certain threshold delimited by the wind parameters. Fig. 10 shows the bolometric luminosity versus M_{BH} diagram for our sample (large symbols), excluding the sources for which $\lambda_{\text{Edd}} > -2.5$. Note that although these sources are mostly CT at this Eddington rate, it is difficult to assess how many sources we may be missing due to the selection biases we have imposed and to the available data.

As a comparison sample, we also plot data from the *Swift*/BAT sample (Koss *et al.* 2017, plotted as the small star symbols). We selected sources from that sample such that they had some estimate on the M_{BH} , with reported values for the intrinsic 2-10 keV luminosity, to obtain the bolometric luminosity and LOS obscuration. We discarded sources without constrained $\log(N_{\text{H}})$ values and we also neglect the sources in common. We obtained a total of 195 sources for the comparison sample. Note that all our sources fall within the region in which the BLR/torus may or may not exist (red lines), according to Elitzur and Netzer (2016). We also plot with red triangles our 11 candidates for the torus disappearance. The location of our candidates is in complete agreement with the idea that the torus disappearance does not rely solely on the bolometric luminosity of the source, yet, it does disappear for inefficient sources. Moreover, González-Martín *et al.* (2017) study a sample of AGN using mid-IR

¹¹ The spectra of M 88 show calibration issues clearly visible in Fig. 5 and resulting in a calibration factor much larger than for the rest of the sample, with a value of $C_{\text{cross}} = 1.99 \pm 0.19$.

$\log(\lambda_{\text{Edd}})$ (total)	Unobs. # (%)	Obs # (%)	CT # (%)	No ref. # (%)
(1)	(2)	(3) (4)	(5)	
-5 (7)	2 (28)	4 (57)	1 (14)	2 (28)
-4 (19)	6 (31)	11 (58)	2 (10)	4 (21)
-3 (41)	3 (7)	28 (68)	10 (24)	3 (7)

Table 5. Number of unobscured, obscured, CT and no reflection sources per Eddington rate range. In parenthesis it is represented the contribution percentage for each of the classifications. Note that sources with no reflection do not sum up to the total contribution in each range, since both the N_{H} classification is independent.

spectra trying to understand the behaviour of the torus in what is called the gradual resizing. We plot in Fig. 10 (gray circles) their candidates for the disappearance of the torus from a mid-IR point of view. Unlike us, they do have objects lacking the torus below the limit proposed by Elitzur and Netzer (2016), at $\lambda_{\text{Edd}} = 10^{-6} - 10^{-5}$ depending on the M_{BH} . However, they also found several candidates in the range between $\lambda_{\text{Edd}} = 10^{-5} - 10^{-3}$. Our study complements theirs by the inclusion of these 11 new candidates to the torus disappearance; all together a sample of 25 AGN. Indeed, we may also be missing objects with $\lambda_{\text{Edd}} < 10^{-5.5}$, either because observations for such low-luminosity objects have not yet been performed, or because the S/N of the observations are so low that they do not fulfill our selection criteria. Moreover, highly obscured objects might be missing because they are more difficult to detect than unobscured objects.

Another interesting result on the obscurer behaviour is the increase on the narrow FeK α line luminosity compared to the reflection luminosity when the reflection luminosity decreases (Fig. 6, large right panel). This is present when we compare the reflection luminosity with the intrinsic luminosity, showing a mean contribution of 40% of reflection for the full range of the intrinsic luminosity (Fig. 6, large left panel). However, the FeK α line and reflection component changes are not associated with the accretion rate, because no correlation is found between the accretion rate and the luminosity of the reflection component or the FeK α line. Although the flux of the narrow FeK α line (compared to the intrinsic X-ray flux) is generally weaker in type-2 AGN than in type-1 AGN for the same 10-50 keV continuum luminosity (Ricci *et al.* 2014), this is not reproduced by the low accretion AGN in our sample. Ricci *et al.* (2014) suggest that this difference can be explained by means of different average inclination angles with respect to the torus, as predicted by the unified model. However, our sample is mostly constituted by type-2 AGN which might explain why we do not find such behaviour. While the FeK α line can be produced by material with column densities as low as $N_{\text{H}} \approx 10^{21-23} \text{ cm}^{-2}$, the Compton hump can only be created by the reprocessing of X-ray photons in CT material. Thus, the increase on the fraction of FeK α line luminosity compared to the Compton hump luminosity toward low reflection luminosities might be an indication of a higher fraction of the emission produced in Compton-thin material associated with the accretion disk. If the accretion disk contribution is responsible for this behaviour, we might expect differences on the photon index distributions that might contribute to the Compton hump and or the FeK α line differently as long as the reflection luminosity decreases. For instance, it is expected for the photon index of standard disks to be larger for higher intrinsic luminosities (softer-when-brighter), while it is expected to decrease with increasing luminosity in radiatively inefficient accretion disks (harder-when-brighter, Narayan and Yi 1995; Connolly *et al.* 2016, and references therein).

However, the mean of the distribution of the photon index

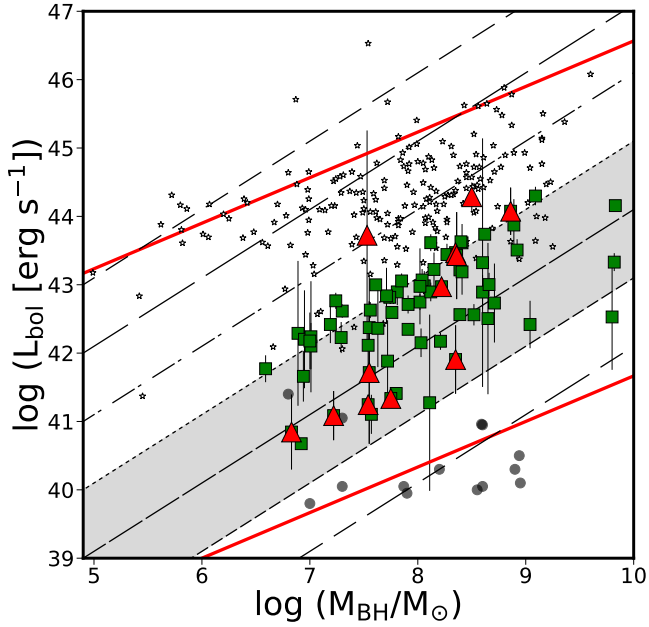


Figure 10. Bolometric luminosity versus M_{BH} for our sample (colors and symbols as in Fig. 6) and the BASS sample (small empty stars). Our 11 candidates are plotted in the larger red triangles. The semi-transparent circles represent the candidates for torus disappearance found by González-Martín *et al.* (2017) using mid-IR data. The black dashed lines represent $\log(L_{\text{Edd}}) = [0, -1, -2, -3, -4, -5, -6]$ from top to bottom, respectively. The two red lines enclose the region in which the torus may or may not exist depending on the wind parameters, as proposed by Elitzur and Ho (2009). The gray-shaded area corresponds to the Eddington rates from the sample not biased by the selection criteria. Note that those sources with Eddington rates above $\log \lambda_{\text{Edd}} \sim -2.5$ are not shown in this plot since at those Eddington rates our sample is not complete.

($\langle \Gamma \rangle = 1.81$) is similar to the average photon index found in diverse AGN samples (e.g. *Swift*/BAT, Koss *et al.* 2017), and we do not find any particular trend on the accretion disk that might explain this behaviour found in the strength of the line. Another alternative is a smooth transition on the average iron abundances of the X-ray reflector (i.e. torus, Ricci *et al.* 2014). This might imply a smooth transition on the chemistry of the torus as seen at X-rays as long as the torus luminosity decreases traced by the Compton hump. In favor, González-Martín *et al.* (2017) also find that a group of objects with a low contribution from the torus, are not well described with the clumpy torus model at mid-IR. They suggest that this might imply that the torus chemistry may be different at low luminosities, consistent with these findings.

6 SUMMARY AND CONCLUSIONS

We have performed an analysis aimed to find the conditions for the change and plausible disappearance of the obscuring gas for low-accretion AGN. For that purpose, we used a sample of 81 sources observed with *NuSTAR* selected by having Eddington rates $\lambda_{\text{Edd}} \lesssim 10^{-3}$. We fitted the data with a model accounting for a patchy absorber and a reflection component from neutral material. We found that $\sim 80\%$ of our sample is obscured, with 20% of CT sources, in agreement with several works (e.g. Ricci *et al.* 2017; Marchesi *et al.* 2018).

In order to directly compare the lack of reflection component with

those sources lacking of the torus at mid-IR wavelengths, fainter X-ray sources, with luminosities $L_X \sim 10^{38} \text{ erg s}^{-1}$ are required. However, we found that a small number of sources in our sample ($\sim 15\%$) seem to lack the reflection component associated with the torus, while the rest of the sources are found to have reflection features such as the existence of the $\text{FeK}\alpha$ line and/or the reflection hump. The sources lacking of reflection component features are located in the region where the torus may or may not disappear according to their M_{BH} and bolometric luminosities. When the reflection component was detected, it accounts for 40% of the luminosity of the intrinsic continuum. We also found tentative evidence in favour of an increase of unobscured sources and a change of the reflector chemistry toward $\lambda_{\text{Edd}} \sim 10^{-5}$. Our findings are in agreement with the scenario in which as the AGN becomes less efficient, the torus is not supported by the radiation field from the wind coming off the accretion disk and fades. As a final remark, we highlight the importance of better S/N data and a broader energy coverage in order to apply more complex models for the reflection component, which includes testing if it may also be produced in the accretion disk (i.e., ionized reflection), but also testing different geometries and matter distributions (i.e. homogeneous, clumpy, etc).

ACKNOWLEDGEMENTS

We thank the anonymous referee for her/his useful comments which greatly improved this paper. This research has made use of the NASA/IPAC Extragalactic Database (NED), which is operated by the Jet Propulsion Laboratory, California Institute of Technology, under contract with the National Aeronautics and Space Administration. This research has made use of data and/or software provided by the High Energy Astrophysics Science Archive Research Center (HEASARC), which is a service of the Astrophysics Science Division at NASA/GSFC and the High Energy Astrophysics Division of the Smithsonian Astrophysical Observatory. NOC would like to thank CONAcYt scholarship No. 897887. CVC acknowledges support from CONAcYt. We thank the UNAM PAPIIT project IN105720 (PI OGM). LHG acknowledges funds by ANID – Millennium Science Initiative Program – ICN12_009 awarded to the Millennium Institute of Astrophysics (MAS).

DATA AVAILABILITY

The data underlying this article are available in at <https://heasarc.gsfc.nasa.gov/>. The datasets were derived from sources in the public domain.

REFERENCES

- Annun, A., Gandhi, P., Alexander, D.M., Lansbury, G.B., Arévalo, P., Balantyne, D.R., and, ...: 2015, *The Astrophysical Journal* 815, 36.
- Annun, A., Alexander, D.M., Gandhi, P., Lansbury, G.B., Asmus, D., Balantyne, D.R., and, ...: 2017, *The Astrophysical Journal* 836, 165.
- Annun, A., Alexander, D.M., Gandhi, P., Lansbury, G.B., Asmus, D., Baloković, M., and, ...: 2020, *Monthly Notices of the Royal Astronomical Society* 497, 229. doi:10.1093/mnras/staa1820.
- Antonucci, R.: 1993, *Annual Review of Astronomy and Astrophysics* 31, 473. doi:10.1146/annurev.aa.31.090193.002353.
- Awaki, H., Koyama, K., Inoue, H., and Halpern, J.P.: 1991, *Publications of the Astronomical Society of Japan* 43, 195.

- Baloković, M., Comastri, A., Harrison, F.A., Alexander, D.M., Ballantyne, D.R., Bauer, F.E., and, ...: 2014, *The Astrophysical Journal* 794, 111. doi:10.1088/0004-637X/794/2/111.
- Baloković, M., Brightman, M., Harrison, F.A., Comastri, A., Ricci, C., Buchner, J., and, ...: 2018, *The Astrophysical Journal* 854, 42.
- Baloković, M., Harrison, F.A., Madejski, G., Comastri, A., Ricci, C., Annun, A., and, ...: 2020, *The Astrophysical Journal* 905, 41. doi:10.3847/1538-4357/abc342.
- Bär, R.E., Trakhtenbrot, B., Oh, K., Koss, M.J., Wong, O.I., Ricci, C., and, ...: 2019, *Monthly Notices of the Royal Astronomical Society* 489, 3073.
- Bassani, L., Dadina, M., Maiolino, R., Salvati, M., Risaliti, G., Della Ceca, R., and, ...: 1999, *The Astrophysical Journal Supplement Series* 121, 473. doi:10.1086/313202.
- Brightman, M. and Nandra, K.: 2008, *Monthly Notices of the Royal Astronomical Society* 390, 1241. doi:10.1111/j.1365-2966.2008.13841.x.
- Brightman, M., Baloković, M., Stern, D., Arévalo, P., Ballantyne, D.R., Bauer, F.E., and, ...: 2015, *The Astrophysical Journal* 805, 41. doi:10.1088/0004-637X/805/1/41.
- Connolly, S. D., McHardy, I. M., Skipper, C. J., & Emmanoulopoulos, D. 2016, *MNRAS*, 459, 3963
- Constantin, A., Green, P., Aldcroft, T., et al. 2009, *ApJ*, 705, 1336
- Dauser, T., García, J., Parker, M.L., Fabian, A.C., and Wilms, J.: 2014, *Monthly Notices of the Royal Astronomical Society* 444, L100.
- de Jong, S., Beckmann, V., Soldi, S., Tramacere, A., and Gros, A.: 2015, *Monthly Notices of the Royal Astronomical Society* 450, 4333. doi:10.1093/mnras/stv927.
- Elitzur, M., and Shlosman, I.: 2006, *The Astrophysical Journal* 648, L101.
- Elitzur, M., and Ho, L.C.: 2009, *The Astrophysical Journal* 701, L91.
- Elitzur, M. and Netzer, H.: 2016, *Monthly Notices of the Royal Astronomical Society* 459, 585.
- Elvis, M.: 2000, *The Astrophysical Journal* 545, 63. doi:10.1086/317778.
- Esparza-Arredondo, D., González-Martín, O., Dultzin, D., Ramos Almeida, C., Fritz, J., Masegosa, J., and, ...: 2019, *The Astrophysical Journal* 886, 125. doi:10.3847/1538-4357/ab4ced.
- Esparza-Arredondo, D., Gonzalez-Martín, O., Dultzin, D., Masegosa, J., Ramos-Almeida, C., García-Bernetete, I., and, ...: 2021, *Astronomy and Astrophysics* 651, A91. doi:10.1051/0004-6361/202040043.
- Ezhikode, S.H., Dewangan, G.C., Misra, R., and Philip, N.S.: 2020, *Monthly Notices of the Royal Astronomical Society* 495, 3373.
- Gebhardt, K., Bender, R., Bower, G., Dressler, A., Faber, S.M., Filippenko, A.V., and, ...: 2000, *The Astrophysical Journal* 539, L13.
- Ferrarese, L. and Merritt, D.: 2000, *The Astrophysical Journal* 539, L9.
- Furui, S., Fukazawa, Y., Odaka, H., Kawaguchi, T., Ohno, M., and Hayashi, K.: 2016, *The Astrophysical Journal* 818, 164.
- González-Martín, O., Masegosa, J., Márquez, I., Guainazzi, M., and Jiménez-Bailón, E.: 2009, *Astronomy and Astrophysics* 506, 1107.
- González-Martín, O., Masegosa, J., Márquez, I., Rodríguez-Espinosa, J.M., Acosta-Pulido, J.A., Ramos Almeida, C., and, ...: 2015, *Astronomy and Astrophysics* 578, A74. doi:10.1051/0004-6361/201425254.
- González-Martín, O., Masegosa, J., Hernán-Caballero, A., Márquez, I., Ramos Almeida, C., Alonso-Herrero, A., Aretxaga, I., Rodríguez-Espinosa, J.M., Acosta-Pulido, J.A., Hernández-García, L., Esparza-Arredondo, D., Martínez-Paredes, M., Bonfini, P., and, ...: 2017, *The Astrophysical Journal* 841, 37.
- Gu, M., & Cao, X. 2009, *MNRAS*, 399, 349
- Guainazzi, M., Matt, G., and Perola, G.C.: 2005, *Astronomy and Astrophysics* 444, 119. doi:10.1051/0004-6361:20053643.
- Gültekin, K., Cackett, E. M., Miller, J. M., et al. 2012, *ApJ*, 749, 129
- Hardcastle, M.J., Worrall, D.M., Kraft, R.P., Forman, W.R., Jones, C., and Murray, S.S.: 2003, *The Astrophysical Journal* 593, 169. doi:10.1086/376519.
- Harrison, F.A., Craig, W.W., Christensen, F.E., Hailey, C.J., Zhang, W.W., Boggs, S.E., and, ...: 2013, *The Astrophysical Journal* 770, 103. doi:10.1088/0004-637X/770/2/103.
- Hernández-García, L., Masegosa, J., González-Martín, O., and Márquez, I.: 2015, *Astronomy and Astrophysics* 579, A90. doi:10.1051/0004-6361/201526127.
- Hernández-García, L., Masegosa, J., González-Martín, O., Márquez, I., and Perea, J.: 2016, *The Astrophysical Journal* 824, 7. doi:10.3847/0004-637X/824/1/7.
- Ikedda, S., Awaki, H., and Terashima, Y.: 2009, *The Astrophysical Journal* 692, 608. doi:10.1088/0004-637X/692/1/608.
- Jang, I., Gliozzi, M., Hughes, C., & Titarchuk, L. 2014, *MNRAS*, 443, 72
- Kalberla, P.M.W., Burton, W.B., Hartmann, D., Arnal, E.M., Bajaja, E., Moras, R., and Poeppel, W.G.L.: 2005, *VizieR Online Data Catalog*, VIII/76.
- Kang, J., Wang, J., and Kang, W.: 2020, *The Astrophysical Journal* 901, 111. doi:10.3847/1538-4357/abdf5.
- Kawamuro, T., Ueda, Y., Tazaki, F., Terashima, Y., and Mushotzky, R.: 2016, *The Astrophysical Journal* 831, 37.
- Arnaud, K.A.: 1996, *Astronomical Data Analysis Software and Systems V* 101, 17.
- Khim, H. and Yi, S.K.: 2017, *The Astrophysical Journal* 846, 155.
- Khorunzhev, G.A., Sazonov, S.Y., Burenin, R.A., and Tkachenko, A.Y.: 2012, *Astronomy Letters* 38, 475.
- Koss, M., Trakhtenbrot, B., Ricci, C., Lamperti, I., Oh, K., Berney, S., Schawinski, K., Baloković, M., Baronchelli, L., Crenshaw, D.M., Fischer, T., Gehrels, N., Harrison, F., and, ...: 2017, *The Astrophysical Journal* 850, 74.
- La Caria, M.-M., Vignali, C., Lanzuisi, G., Gruppioni, C., and Pozzi, F.: 2019, *Monthly Notices of the Royal Astronomical Society* 487, 1662. doi:10.1093/mnras/stz1381.
- Laor, A.: 2001, *The Astrophysical Journal* 553, 677.
- Laor, A.: 2003, *The Astrophysical Journal* 590, 86.
- Leahy, D.A. and Creighton, J.: 1993, *Monthly Notices of the Royal Astronomical Society* 263, 314. doi:10.1093/mnras/263.2.314.
- Liu, Y. and Li, X.: 2014, *The Astrophysical Journal* 787, 52. doi:10.1088/0004-637X/787/1/52.
- Magdziarz, P., and Zdziarski, A.A.: 1995, *Monthly Notices of the Royal Astronomical Society* 273, 837.
- Marchesi, S., Ajello, M., Marcotulli, L., Comastri, A., Lanzuisi, G., and Vignali, C.: 2018, *The Astrophysical Journal* 854, 49. doi:10.3847/1538-4357/aaa410.
- Marchesi, S., Ajello, M., Zhao, X., Marcotulli, L., Baloković, M., Brightman, M., and, ...: 2019, *The Astrophysical Journal* 872, 8. doi:10.3847/1538-4357/aafbeb.
- Marconi, A., Risaliti, G., Gilli, R., Hunt, L.K., Maiolino, R., and Salvati, M.: 2004, *Monthly Notices of the Royal Astronomical Society* 351, 169.
- Matt, G., Guainazzi, M., and Maiolino, R.: 2003, *Monthly Notices of the Royal Astronomical Society* 342, 422.
- McKernan, B., Ford, K.E.S., and Reynolds, C.S.: 2010, *Monthly Notices of the Royal Astronomical Society* 407, 2399.
- Merloni, A., Bongiorno, A., Brusa, M., Iwasawa, K., Mainieri, V., Magnelli, B., and, ...: 2014, *Monthly Notices of the Royal Astronomical Society* 437, 3550. doi:10.1093/mnras/stt2149.
- Molina, M., Malizia, A., Bassani, L., Ursini, F., Bazzano, A., and Ubertaini, P.: 2019, *Monthly Notices of the Royal Astronomical Society* 484, 2735.
- Murphy, K.D. and Yaqoob, T.: 2009, *Monthly Notices of the Royal Astronomical Society* 397, 1549. doi:10.1111/j.1365-2966.2009.15025.x.
- Nandra, K., O'Neill, P.M., George, I.M., and Reeves, J.N.: 2007, *Monthly Notices of the Royal Astronomical Society* 382, 194.
- Narayan, R. and Yi, I.: 1995, *The Astrophysical Journal* 452, 710. doi:10.1086/176343.
- Nemmen, R.S., Storchi-Bergmann, T., and Eracleous, M.: 2014, *Monthly Notices of the Royal Astronomical Society* 438, 2804. doi:10.1093/mnras/stt2388.
- Netzer, H.: 2015, *Annual Review of Astronomy and Astrophysics* 53, 365.
- Oda, S., Tanimoto, A., Ueda, Y., Imanishi, M., Terashima, Y., and Ricci, C.: 2017, *The Astrophysical Journal* 835, 179. doi:10.3847/1538-4357/835/2/179.
- Panagiotou, C. and Walter, R.: 2019, *Astronomy and Astrophysics* 626, A40.
- Panagiotou, C. and Walter, R.: 2020, *Astronomy and Astrophysics* 640, A31. doi:10.1051/0004-6361/201937390.
- Panessa, F., Bassani, L., Cappi, M., Dadina, M., Barcons, X., Carrera, F.J., Ho, L.C., and Iwasawa, K.: 2006, *Astronomy and Astrophysics* 455, 173.
- Peterson, B. M. 1997, *An introduction to active galactic nuclei*, Publisher: Cambridge, New York Cambridge University Press, 1997 Physical de-

- scription xvi, 238 p. ISBN 0521473489,
- Ramos Almeida, C., Levenson, N.A., Rodríguez Espinosa, J.M., Alonso-Herrero, A., Asensio Ramos, A., Radomski, J.T., and, ...: 2009, *The Astrophysical Journal* 702, 1127.
- Ramos Almeida, C. and Ricci, C.: 2017, *Nature Astronomy* 1, 679.
- Ricci, C., Walter, R., Courvoisier, T.J.-L., and Paltani, S.: 2011, *Astronomy and Astrophysics* 532, A102.
- Ricci, C., Ueda, Y., Paltani, S., Ichikawa, K., Gandhi, P., and Awaki, H.: 2014, *Monthly Notices of the Royal Astronomical Society* 441, 3622. doi:10.1093/mnras/stu735.
- Ricci, C., Ueda, Y., Koss, M.J., Trakhtenbrot, B., Bauer, F.E., and Gandhi, P.: 2015, *The Astrophysical Journal* 815, L13. doi:10.1088/2041-8205/815/1/L13.
- Ricci, C., Trakhtenbrot, B., Koss, M.J., Ueda, Y., Schawinski, K., Oh, K., and, ...: 2017, *Nature* 549, 488. doi:10.1038/nature23906.
- Shakura, N.I. and Sunyaev, R.A.: 1973, *Astronomy and Astrophysics* 500, 33.
- Tadhunter, C. and Tsvetanov, Z.: 1989, *Nature* 341, 422. doi:10.1038/341422a0.
- Tanimoto, A., Ueda, Y., Kawamuro, T., Ricci, C., Awaki, H., and Terashima, Y.: 2018, *The Astrophysical Journal* 853, 146. doi:10.3847/1538-4357/aaa47c.
- Tanimoto, A., Ueda, Y., Odaka, H., Kawaguchi, T., Fukazawa, Y., and Kawamuro, T.: 2019, *The Astrophysical Journal* 877, 95. doi:10.3847/1538-4357/ab1b20.
- Tanimoto, A., Ueda, Y., Odaka, H., Ogawa, S., Yamada, S., Kawaguchi, T., and, ...: 2020, *The Astrophysical Journal* 897, 2. doi:10.3847/1538-4357/ab96bc.
- Tran, H.D.: 2001, *The Astrophysical Journal* 554, L19. doi:10.1086/320926.
- Urry, C. M., & Padovani, P. 1995, *PASP*, 107, 803
- van den Bosch, R.C.E., Gebhardt, K., Gültekin, K., Yıldırım, A., and Walsh, J.L.: 2015, *The Astrophysical Journal Supplement Series* 218, 10.
- Ursini, F., Bassani, L., Panessa, F., Bazzano, A., Bird, A.J., Malizia, A., and, ...: 2018, *Monthly Notices of the Royal Astronomical Society* 474, 5684. doi:10.1093/mnras/stx3159.
- van den Bosch, R.C.E.: 2016, *The Astrophysical Journal* 831, 134.
- Vasudevan, R.V. and Fabian, A.C.: 2009, *Monthly Notices of the Royal Astronomical Society* 392, 1124.
- Woo, J.-H., and Urry, C.M.: 2002, *The Astrophysical Journal* 581, L5.
- Younes, G., Porquet, D., Sabra, B., & Reeves, J. N. 2011, *A&A*, 530, A149
- Younes, G., Ptak, A., Ho, L.C., Xie, F.-G., Terasima, Y., Yuan, F., and, ...: 2019, *The Astrophysical Journal* 870, 73.
- Zhao, X., Marchesi, S., Ajello, M., Marcotulli, L., Cusumano, G., La Parola, V., and, ...: 2019, *The Astrophysical Journal* 870, 60. doi:10.3847/1538-4357/aaf1a0.

APPENDIX A: MODELING WITH CABS

We use a model which does not account for the Compton scattering, particularly important for Compton-thick objects (Annuar *et al.* 2017; Ricci *et al.* 2017; Zhao *et al.* 2019; Marchesi *et al.* 2019). XSPEC has a model to account for Compton scattering called `cabs`¹². This model component has been reported to present some issues (see e.g. MYTORUS manual and Tanimoto *et al.* 2018), and does not emulate properly the X-ray spectra of AGN. However, `cabs` has been used in several recent works to account for Compton scattering in AGN when using *NuSTAR* data (see Ricci *et al.* 2017; Oda *et al.* 2017; Tanimoto *et al.* 2020). In practice, we added the `cabs` component to the model in Eq. (4) as follows:

$$M_5 = \text{phabs}_{\text{Gal}}((\text{zphabs}_{\text{intr}} * \text{cabs} * \text{zpower1w}) + \text{ct} * \text{zpower1w} + \text{pexmon} + \text{zgauss}_{6.7 \text{ keV}} + \text{zgauss}_{6.97 \text{ keV}}) \quad (\text{A1})$$

¹² see XSPEC manual <https://heasarc.gsfc.nasa.gov/xanadu/xspec/manual/XspecManual.html>

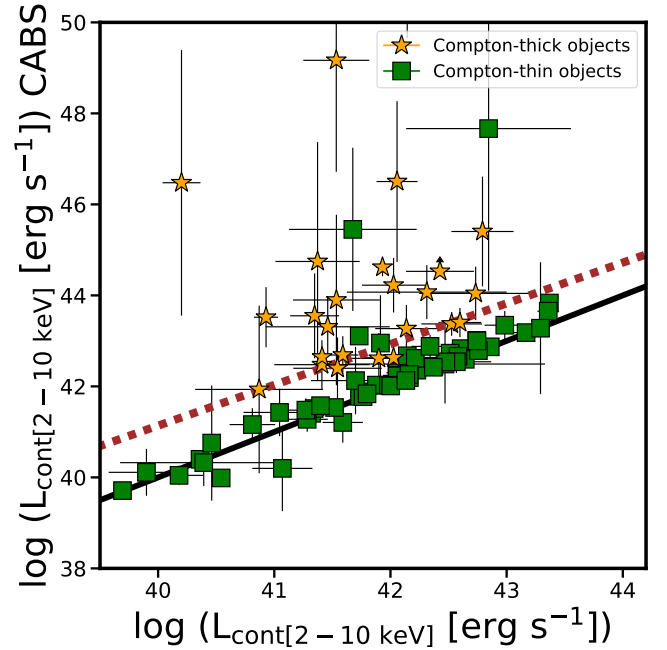


Figure A1. Intrinsic luminosity of the power-law component when including `cabs` in the spectral modeling (vertical axis) compared to the case in which it is not used (horizontal axis). The brown dotted and black solid lines are the best fit to the data and the 1:1 relation, respectively.

letting the N_{H} in the `cabs` component to be the same as that of the LOS obscuration. The resulting N_{H} values are mostly consistent with those reported in this work (see below). However, the intrinsic luminosity of the sources obtained for some objects changes by a factor of 10^4 (see Fig. A1 shows). Indeed, note that a non-negligible amount of sources fall well outside the 1:1 relation even when accounting for error bars (black solid line). Moreover, the error bars are much larger when using `cabs` than when excluding it. These luminosities result in Eddington rates close to the Eddington limit, which are unrealistic values for LLAGN.

These results imply that there is a systematic uncertainty when adding the Compton-scattering through the `cabs` component. However, this does not imply that such a component does not physically exist in the X-ray spectra of AGN. In fact, the neglect of this component does add a systematic uncertainty to the general analysis. Indeed, this effect primarily affects the X-ray spectra of CT objects. Thus, although the addition of `cabs` does not lead to physically realistic results, the exclusion of the Compton-scattering effects in our analysis, imply that all intrinsic luminosities for CT sources reported here should be treated as lower limits.

We have also checked how the exclusion of this component affects the N_{H} measurement. Fig. A2 shows the change in this parameter. The black dashed line shows the 1:1 relation. In this case, most of the sources fall in this line, with only 8 sources falling outside the relation. Note that this is a result similar to the one by Tanimoto *et al.* (2018, see their Fig. 5a), where they found larger values for the intrinsic luminosity when using this model. However, the spectral parameters were not very much affected.

This paper has been typeset from a \LaTeX file prepared by the author.

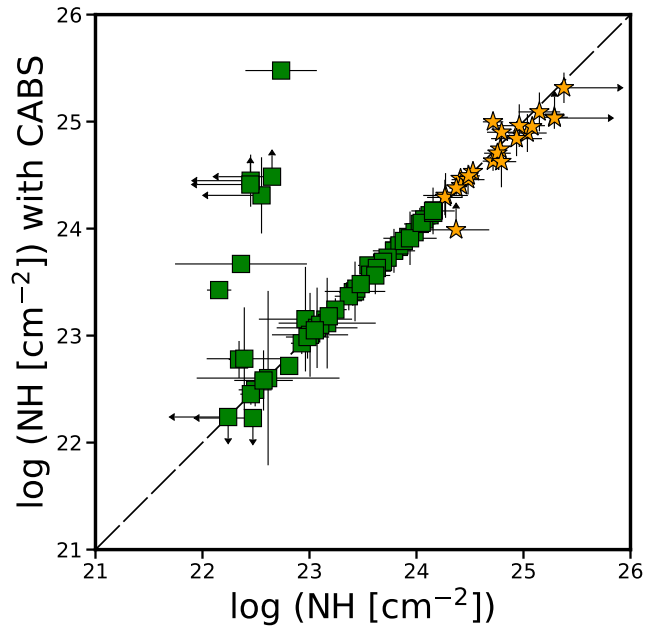


Figure A2. Column density of the sources when *cabs* is added (vertical axis) compared to the case in which it is not used (horizontal axis). The black dashed line is the 1:1 relation.